ARL-TR-7252 • MAR 2015

US Army Research Laboratory

Metamaterial and Metastructural Architectures for Novel C4ISR Devices and Sensors

by Weimin Zhou, Gerard Dang, Monica Taysing-Lara, Daniel Shreiber, Melanie Cole, Eric Ngo, Matt Ivill, Grace Metcalfe, Nathaniel Woodward, and Amir Zaghloul

NOTICES

Disclaimers

The findings in this report are not to be construed as an official Department of the Army position unless so designated by other authorized documents.

Citation of manufacturer's or trade names does not constitute an official endorsement or approval of the use thereof.

Destroy this report when it is no longer needed. Do not return it to the originator.

ARL-TR-7252 ● MAR 2015

US Army Research Laboratory

Metamaterial and Metastructural Architectures for Novel C4ISR Devices and Sensors

by Weimin Zhou, Gerard Dang, Monica Taysing-Lara, Grace Metcalfe, Nathaniel Woodward, and Amir Zaghloul
Sensors and Electron Devices Directorate

Daniel Shreiber
Oak Ridge Institute for Science and Education
Belcamp, MD

Melanie Cole, Eric Ngo, and Matt Ivill
Weapons and Materials Research Directorate

REPORT DOCUMENTATION PAGE

Form Approved
OMB No. 0704-0188

1. REPORT DATE *(DD-MM-YYYY)*	2. REPORT TYPE	3. DATES COVERED (From - To)
March 2015	DSI	2012–2014

4. TITLE AND SUBTITLE
Metamaterial and Metastructural Architectures for Novel C4ISR Devices and Sensors

5a. CONTRACT NUMBER

5b. GRANT NUMBER

5c. PROGRAM ELEMENT NUMBER

6. AUTHOR(S)
Weimin Zhou, Gerard Dang, Monica Taysing-Lara, Daniel Shreiber, Melanie Cole, Eric Ngo, Matt Ivill, Grace Metcalfe, Nathaniel Woodward, and Amir Zaghloul

5d. PROJECT NUMBER

5e. TASK NUMBER

5f. WORK UNIT NUMBER

7. PERFORMING ORGANIZATION NAME(S) AND ADDRESS(ES)
US Army Research Laboratory
ATTN: RDRL-SEE-E
2800 Powder Mill Road
Adelphi, MD 20783-1197

8. PERFORMING ORGANIZATION REPORT NUMBER
ARL-TR-7252

9. SPONSORING/MONITORING AGENCY NAME(S) AND ADDRESS(ES)

10. SPONSOR/MONITOR'S ACRONYM(S)

11. SPONSOR/MONITOR'S REPORT NUMBER(S)

12. DISTRIBUTION/AVAILABILITY STATEMENT
Approved for public release; distribution unlimited.

13. SUPPLEMENTARY NOTES

14. ABSTRACT
We have developed novel metamaterial devices and metastructures with new electronic and optoelectronic (OE) properties and used them to design and fabricate devices, such as slow-light, low-loss waveguides, terahertz modulators, and wideband radio frequency (RF) antennas with new functionalities. These devices will provide basic building blocks for future chip-scale semiconductor-integrated OE circuits and provide new capabilities over a wide range of frequencies from microwaves, terahertz, and into the infrared in Command, Control, Communications, Computers, Intelligence, Surveillance and Reconnaissance systems. We focused on 3 different types of metamaterial devices as basic building blocks. These are low-loss, slow-light, hollow-core metastructure waveguides for chip-scale-integrated OE/RF photonic circuit; metamaterial devices for terahertz communication/sensing/imaging; and tunable RF metamaterials. Some of our major accomplishments in this area of study include developing and demonstrating the world's first silicon-based slow-light metastructure hollow-core waveguide, developing and demonstrating new tunable terahertz metamaterial devices, and designing and fabricating terahertz metastructure hollow-core waveguide. The DSI project has resulted in 14 publications, 1 US patent, 1 invention disclosure, and 1 press release.

15. SUBJECT TERMS
metamaterial, metastructure, devices, terahertz, hollow-core waveguide

16. SECURITY CLASSIFICATION OF:			17. LIMITATION OF ABSTRACT	18. NUMBER OF PAGES	19a. NAME OF RESPONSIBLE PERSON
a. REPORT	b. ABSTRACT	c. THIS PAGE			Weimin Zhou
Unclassified	Unclassified	Unclassified	UU	76	19b. TELEPHONE NUMBER (Include area code) 301-394-1435

Contents

List of Figures

Acknowledgments

We acknowledge our university collaborators, Prof Connie Chang-Hasnain, Dr Vadim Karagodsky, Tianbo Sun, and Dr Weijian Yang from the University of California at Berkeley, and Dr Phillippe Lalanne from Institut d'Optique (France) for their contribution of theoretical modelling and simulation for the metastructure hollow-core waveguides.

We thank Dr Larry Stout, Dr Steve Weiss, and Dr Mike Wraback for their administrative guidance.

INTENTIONALLY LEFT BLANK.

1. Introduction

1.1 Objective

Our objective for this research is to develop novel metamaterial devices and metastructures with new electronic and optoelectronic (OE) properties and use them to design and fabricate devices, such as slow-light, low-loss waveguides, terahertz modulators, and wideband radio frequency (RF) antennas with new functionalities. These devices will provide basic building blocks for future chip-scale semiconductor-integrated OE circuits and provide new capabilities over a wide range of frequencies from microwaves, terahertz, and into the infrared in Command, Control, Communications, Computers, Intelligence, Surveillance, and Reconnaissance (C4ISR) systems.

1.2 Approach

We are focusing on 3 different types of metamaterial devices as basic building blocks:

- *Low-loss, slow-light, hollow-core metastructure waveguides for chip-scale-integrated OE/RF photonic circuits (EO&P, SEDD).* We will use a new type of high-contrast-grating metastructure as "cage"-cladding of a hollow-core waveguide structure to achieve low propagation loss and "slow-light" properties. This can provide a long time delay or an ultra-high *Q* cavity in a small semiconductor chip.
- *Metamaterial devices for terahertz communication/sensing/imaging (SEDD and WMRD).* We will develop an active metamaterial device to control polarization or intensity in the terahertz regime. The active metamaterial is constructed using split-ring resonator unit cells as canonical elements with a tunable capacitor made by complex oxide thin films or photoelectric materials. This device will provide the basic building blocks for future terahertz communication/sensing/imaging applications.
- *Tunable RF metamaterials (RF&E, SEDD).* We will design and characterize tunable metamaterials at RF frequencies through simulations and measurements.

1.3 Major Accomplishments

Some of our major accomplishments in this area of study are as follows:

- *Developed and demonstrated the world's first silicon (Si)-based slow-light metastructure hollow-core waveguide.* We have designed, fabricated, and tested this new type of 3-dimensional (3-D) cage-like metastructure waveguide. As a result, a new and unique fabrication technique was developed in-house. We have experimentally tested several fabricated waveguides to measure the propagation loss and group velocity. We demonstrated propagation losses less than 1 dB/cm at certain wavelengths and a group velocity greater than 0.2c, where c is the speed of light, for slow-light propagation. In collaborating with UC Berkeley and Institute d'Optique (France), we developed a simulation model for this waveguide.
- *Developed and demonstrated new tunable terahertz metamaterial devices.* We have designed several tunable terahertz metamaterial structures containing 3-D metal split-rings with a tunable capacitor fabricated using complex oxide thin films. Subsequently, the team developed a new fabrication technique and successfully fabricated such 3-D tunable metamaterial devices. In addition, a simulation model is developed to assist the metamaterial device design and predict the resonance frequency and tuning. We have finally tested a fabricated device sample in terahertz frequency. The test result is in general agreement with the experimental test.
- *Designed and fabricated terahertz metastructure hollow-core waveguide.* We have successfully designed and fabricated the world's first Si-based metastructure hollow-core waveguide. The waveguide is built using the entire wafer thickness. The waveguides have a round cross-sectional hollow core surrounded by highly reflective cladding walls, which is made by high-contrast metastructure gratings. We developed a new fabrication technique to fabricate such a 3-D metastructure cage-like waveguide structure. The waveguide is aimed for low propagation loss and integration with Si-based integrated circuits for the application in terahertz circuitry for bio/chem sensing or terahertz imaging.
- *The DSI project has resulted in 14 publications, 1 US patent, 1 invention disclosure, and 1 press release.*

2. Slow-Light High-Contrast Metastructure Hollow-Core Waveguide

Gerard Dang, Monica Taysing-Lara, and Weimin Zhou (SEDD)

2.1 Abstract

We have developed a new type of silicon (Si)-based 3-dimensional (3-D) cage-like high-contrast metastructure waveguide with both "slow-light" and low-loss properties, which has applications in providing a long time-delay line or a high *Q* cavity in chip-scale optoelectronic integrated circuits (OEICs). Traditional semiconductor optical waveguides always have high loss when used in a high-dispersion (slow-light) region. A preliminary computational model has predicted that there is a slow-light and low-propagation loss region within cage-like hollow-core waveguides formed by 4 high-contrast-grating (HCG) walls/claddings. Using our new processing technique, we fabricated several such waveguides on an Si wafer with different core sizes/shapes and different HCGs for 1,550 operation wavelength. We have conducted experimental waveguide delay test measurements using a short optical pulse which indicated that the group velocity of these metastructure waveguides are in the range of 20%–30% of the speed of the light. Using a waveguide "cut-back" method, we have experimentally determined the propagation loss of these waveguides is in the range of 2–5 dB/cm. We are also developing this type of high-contrast metastructure hollow-core waveguide for different operating wavelengths/frequencies, such as terahertz, for different applications.

2.2 Introduction

Semiconductor integrated circuits (ICs) and fiber optics are the 2 basic technologies that have made a big impact in our modern lives. In many cases, low-loss long fiber has been used not for sending signals over long physical distances, but rather for providing a long time delay or an ultra-high *Q* cavity. Unfortunately, long fiber spools are large in size and cannot be monolithically integrated with semiconductor IC. If we can create a slow-light, low-loss waveguide with a small form factor on an Si wafer, we can then provide a long time delay or an ultra-high *Q* cavity in a chip scale digital or analog OEIC for many applications, such as a buffered delay for communication or computation system, precision optical or radio frequency (RF) signal sources, optical true-time-delay beamformer for phased array antennas, RF-photonic signal

processors/filters, etc. “Slow-light” is the key to reducing the size of the delay line. Unfortunately, traditional waveguides always have a high propagation loss when used in a high-dispersion wavelength region since loss and dispersion cannot be separated in a homogeneous material.

In recent years, UC Berkeley has found a new type of HCG metastructure that has demonstrated ultra-high reflectivity.[1,2] Therefore, using this type of metagrating as the wall/cladding to build a hollow-core waveguide, as shown in Fig. 2.1, can achieve ultra-low loss because the propagation light cannot escape from the HCG cladding, and there is no absorption loss in the core area.[3–5] The physics of this metagrating are related to resonance created by the artificial unit cell or the geometric arrangement of 2 materials having a high index contrast. This provides us with an opportunity to engineer the HCG metastructure to create a “bending” in the ω-k dispersion curve for the propagation modes in the waveguide. The “bending” causes a “0” slope region in the dispersion curve (“0” group velocity). The challenge is to design the waveguide such that it has both slow-light and low-loss properties in the same operational bandwidth. Hence, such a slow-light waveguide device will be very useful for RF-photonics applications, such as delay lines or building a high-Q-cavity microwave.

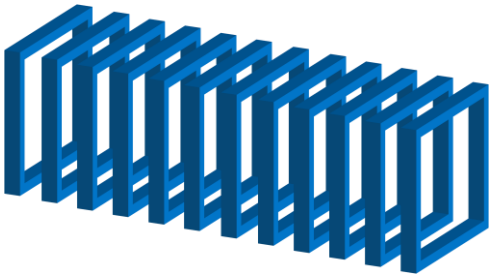

Fig. 2.1 Representation of the meta-HCG 3-D cage hollow-core waveguide structure

The next challenge is to fabricate such a 3-D cage-structure waveguide. Recently, the RF-Photonics team at the US Army Research Laboratory developed a new low-cost fabrication technique to construct the 3-D cage hollow-core waveguide that has HCG metastructures as the 4 cladding/walls of the waveguide,[4,6] all fabricated on a standard Si-on-insulator (SOI) wafer.

In this project, we have to first improve our fabrication technique to reduce the roughness and nonuniformity size variation by comparing and testing different etching techniques, such as modified Bosch etch[4,7] and modified Bosch with isotropic under-cut etch.[8] Since the simplified 2-dimensional (2-D) ideal computation model cannot precisely predict the real case for the 3-D cage-structure waveguide, we had to fabricate several waveguides with different core

sizes/shapes and different HCGs for 1,550 operation wavelength. We have conducted an experimental waveguide delay test using a short optical pulse to measure the group velocity and demonstrate the slow-light property. Using a waveguide "cut-back" method, we have experimentally determined the propagation loss of these waveguides.

2.3 Modeling and Simulation

The goal of this project is to develop the hollow-core waveguide not only for low loss, but also for high dispersion or "slow-light" properties. To design such a waveguide, as shown in Fig. 2.1 we use high-reflection HCG metastructures as the 4 cladding/walls of a squared hollow-core waveguide, where the guided light is approximately 100% reflected from the metagratings, and there is no absorption from the core, therefore resulting in ultra-low loss. Unlike a conventional waveguide, a metastructural waveguide can be engineered to create a phase transition that generates a "0" slope in the dispersion curve (i.e., "0" group velocity). We chose Si-base SOI wafers to make our waveguide for operation wavelength around 1,550 nm; therefore, the waveguide can be monolithically integrated with an Si-based OE circuit and have the advantage of a complementary metal-oxide semiconductor (CMOS)-compatible fabrication process.

We collaborated with Prof Connie Chang-Hasnain's group at UC Berkeley to conduct theoretical simulation and modeling to search a suitable waveguide structure that has both low-loss and slow-light effects in the same operational bandwidth.

UC Berkeley's research group has developed a simplified model to simulate such a waveguide with beam propagation between 2 HCGs, as shown in Fig. 2.2. This simplified simulation model is based on 2-D calculation of the high-contrast grating and combining the 2-D result with the hollow-core waveguide simulation. The black dispersion curves represent the propagation modes of a traditional hollow-core slab waveguide with total reflection cladding. The blue curves represent the modes of an HCG metastructure hollow-core slab waveguide. We can see that there is a mode transition between 2 neighboring modes that has a smaller slope. Figure 2.2 (left) shows the 2-D mapping of the computational modeling results of the dispersion curve and loss plot (HCG's reflectivity showing by color) for the propagation modes in this waveguide. Figure 2.2 (right) shows the mapping of the dispersion curves with the phase of the propagation modes, which indicate that the mode hopping (transition) occurs at a π phase transition. By adjusting the core dimension, D, the duty cycle, Λ, and the height of the grating bar, t_g, one can obtain a region that has both "slow-light" (low group velocity) and low-loss properties.

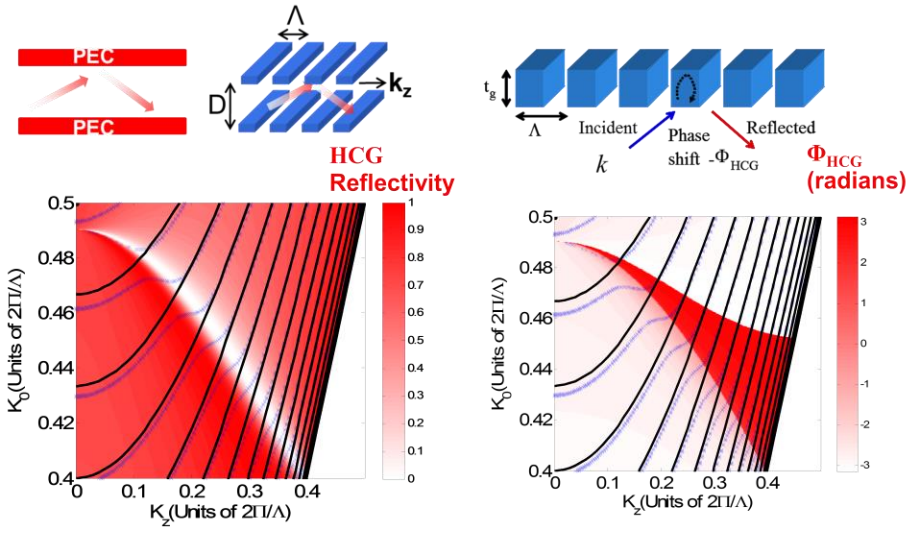

Fig. 2.2 Simulation modeling: the mode hopping due to the phase transition at the meta-HCG causes a flat slope on the dispersion curve, which represents a low group velocity

Figure 2.3 shows the result for D = 1 μm, Λ = 1.5 μm, and a duty cycle of 50/50. Figure 2.4 (left) shows the "zoom-in" plot of the waveguide loss superimposed with the "slow-light" region of the dispersion curve in k-space. Figure 2.4 (right) shows both the loss and the group velocity as a function of frequency. These preliminary modeling results indicate that the group velocity can be as low as 0.02c with very little waveguide loss; the bandwidth of this low-loss region is about 100 GHz. This means such a slow-light waveguide device will be very useful for RF-photonics applications, such as delay lines or building a high-*Q*-cavity microwave.

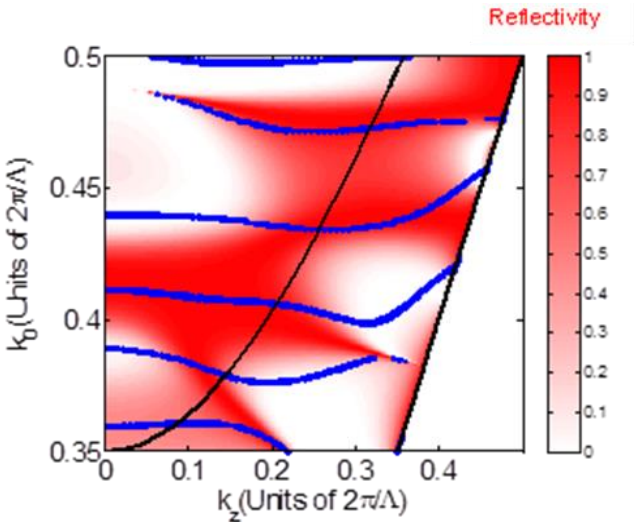

Fig. 2.3 Simulation of a 1-μm core metastructure hollow-core waveguide

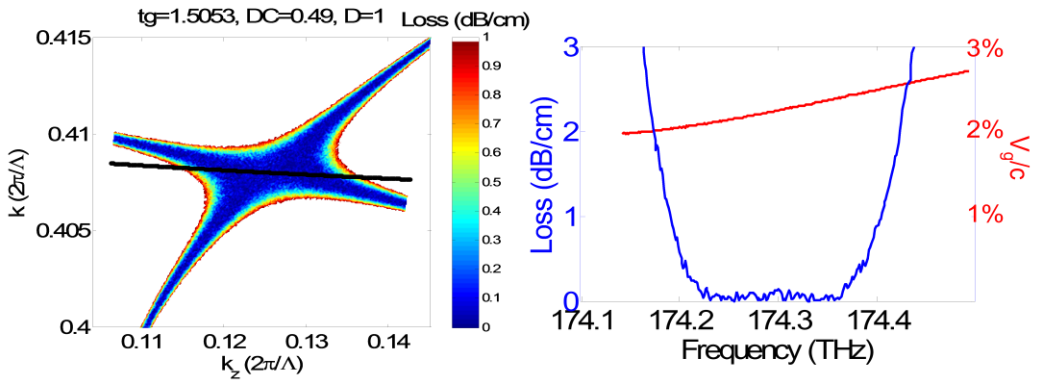

Fig. 2.4 Simulated "slow light" with average 0.02c velocity and 0.1 dB/cm loss over a 100-GHz bandwidth

This simulation result may provide some guidance only for the hollow-core metastructure waveguide's property. A more complex 3-D simulation model is needed to more precisely calculate the dispersion and waveguide loss for this new type of waveguide. More detailed theoretical modeling and simulation will be published elsewhere.

2.4 Design and Fabrication

The goal of this effort is to design and fabricate the metastructure hollow-core waveguide that has both slow-light and low-loss properties. The simplified 2-D ideal computation model for the slab waveguide formed by top and bottom HCGs cannot precisely represent the real case for the 3-D cage-structure waveguide that has 4 HCG walls. A more sophisticated 3-D simulation model is needed to find the optimum slow-light and low-loss region with precise 3-D cage structure's HCG parameters for the 3-D waveguide. However, the simplified 2-D simulation model can provide some hints for guidance. By adjusting the core dimension, D, the duty cycle, Λ, and the height of the grating bar, t_g, one can see the trend of change in the dispersion curve and loss property in the ω-k diagram. Using this guidance, we have designed many of the waveguides for 1,550-nm operation with different dimensions: core sizes D = 1 × 1 μm, 1.5 × 1 μm, 2 × 1.5 μm, and 2 × 2 μm, etc.; period from 0.625 to 0.7 μm; duty cycle from 20/80 to 50/50.

The waveguides are fabricated on SOI wafers so that they can be monolithically integrated with an Si-base OEIC and have the advantage of a CMOS-compatible fabrication process. The cage waveguide is made in the top Si layer. The silicon dioxide (SiO_2) layer under the waveguide region is removed to suspend the cage waveguide. We have designed 3 configurations of the cage waveguide: 1) 5 waveguides per array so that each neighboring waveguide shares the same vertical HCG cladding; 2) single-cage waveguides held by a pair of short arms; and 3)

single-cage waveguides held by a pair of long arms. These single waveguide configurations are designed to promote the input laser light to be coupled into only one hollow-core waveguide and reduce the chance of coupling the light into other waveguides or into the Si slab of the SOI wafer.

2.4.1 Fabrication Methods

Our new fabrication technique can fabricate this 3-D metastructure waveguide from the 2-D surface of the SOI wafer using a self-aligned modified Bosch plasma-etching process without any multilayer deposition, regrowth, multilithography alignments, wafer flip-bonding, etc.[9] The fabrication process uses a 2-D etching mask (which can be made by e-beam lithography) on the top surface of the SOI wafer. The mask pattern comprises a series of parallel lines with line distance equal to the grating pitch, wherein a line width is equal to a high-index grating line width, where the center portion of the line represents the waveguide area, as shown in Fig. 2.5a. Each line comprises at least 2 wider-shaped features, which define the positions of a pair of vertical posts that will form the vertical gratings/claddings for a hollow-core waveguide. Using the 2-D mask for our special modified Bosch etching process (which creates a deep vertical trench with a varying vertical profile [narrow, wide, narrow], as shown in Fig. 2.5b) results in a 3-D metastructural hollow-core waveguide, as shown in Fig. 2.5c.

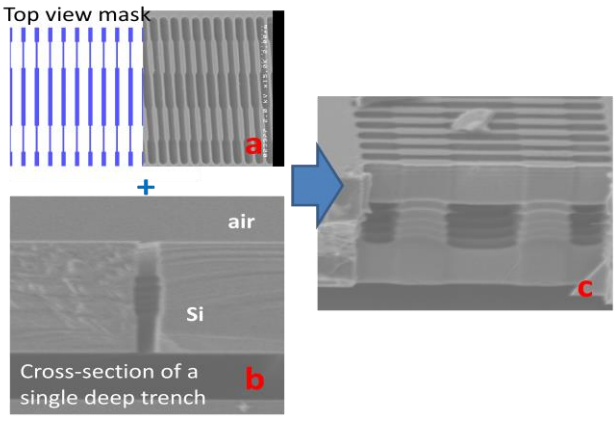

Fig. 2.5 a) Top view of the mask pattern and scanning electron microscope (SEM) picture of the top surface for etched structure; b) SEM picture of the cross section of the deep trench; and c) SEM picture of a 3-D cage waveguide

2.4.1.1 Modified Bosch Etch

To create the narrow, wide, narrow variable vertical trench etching profile, we have first developed a special recipe with a modified Botch etch process to vary the width of the narrow trench while etch down. The Bosch etch process[7] uses a

repetition of 3 steps of either a plasma etch or a deposition cycle to achieve a high-aspect ratio etch in Si with vertical sidewalls. The first step uses polymer passivation to coat the open surface with a thin polymer coating. The second step is a directional etch using high-energy plasma to remove the polymer that is on the bottom of the open surfaces while maintaining a protective polymer layer on the sidewalls of the trench. The third step is an isotropic Si etch. We modified the standard Bosch process to achieve a wider core region in our etch profile by adjusting the isotropic etch effect in order. This modified Bosch etch can undercut the core region under the top HCG to form the hollow core and leave a series of parallel vertical posts to form the vertical metagrating cladding as well as the bottom metagrating. After the dry-etch processes, selective wet buffered hydrogen fluoride (HF) etch is used to remove the SiO_2 layer under the waveguide so that the 3-D hollow-core waveguide is suspended in air.

2.4.1.2 Modified Bosch Etch with Isotropic Undercut Etch

We have developed an alternative etch method to create the narrow, wide, narrow variable vertical trench etching profile, which adapted part of the Single-Crystal silicon REactive etch and Metal (SCREAM) etch process[8] in our modified Bosche etch method. The method involves a few more steps. The first step is to use the regular Bosch etch to etch the trench for the top HCG cladding with the same etch mask. Then, deposit a thin coating of SiO_2 on the etched trench surface using plasma-enhanced chemical vapor deposition (PECVD) or put an additional polymer coating. The next step is to use directional plasma etching to remove the SiO_2 coating (polymer) at the bottom of the trench, then perform another standard Bosch etch to continue the trench by adding a waveguide core height. After that, we use oxygen plasma to remove the polymer coating on the lower part (core region) of the trench and perform an isotropic etching to expand the width of the trench until it undercuts the core region completely. The next step is to repeat another standard Bosch etch to create the bottom HCG/cladding until it reaches the SiO_2 layer of the SOI wafer. The final step is to again perform an HF wet etch to remove the SiO_2 layer under the waveguide.

2.4.2 Comparison

Figure 2.6 shows the scanning electron microscope (SEM) pictures of several high-contrast metastructure hollow-core waveguides fabricated with the modified Bosch method. Figure 2.6a shows a waveguide array, Fig. 2.6b shows a single waveguide with short support arm configuration, and Fig. 2.6c shows a single waveguide with the long-arm support. The advantage of the modified Bosch method is the simplicity of fabrication. The fabrication can be done by a “single”

programmable, cycled, inductance coupled plasma (ICP) etch plus a wet etch with HF. The problem with our modified Bosch etch technique is the scalloping roughness on the vertical walls/posts and a needle bar in the middle of the core, which was created by the shadow effect of the etching. To remove the needle bars and smooth the surface of the HCGs, we performed a thermal oxidization and HF wet etch on our sample. Figure 2.7 shows the waveguide before and after these processes, which removed the unwanted needle bars in the core. However, when the oxidization and HF wet etch process removed a layer of material in every surface, the grating bars became thinner, therefore reducing the duty cycle of the metastructure HCG.

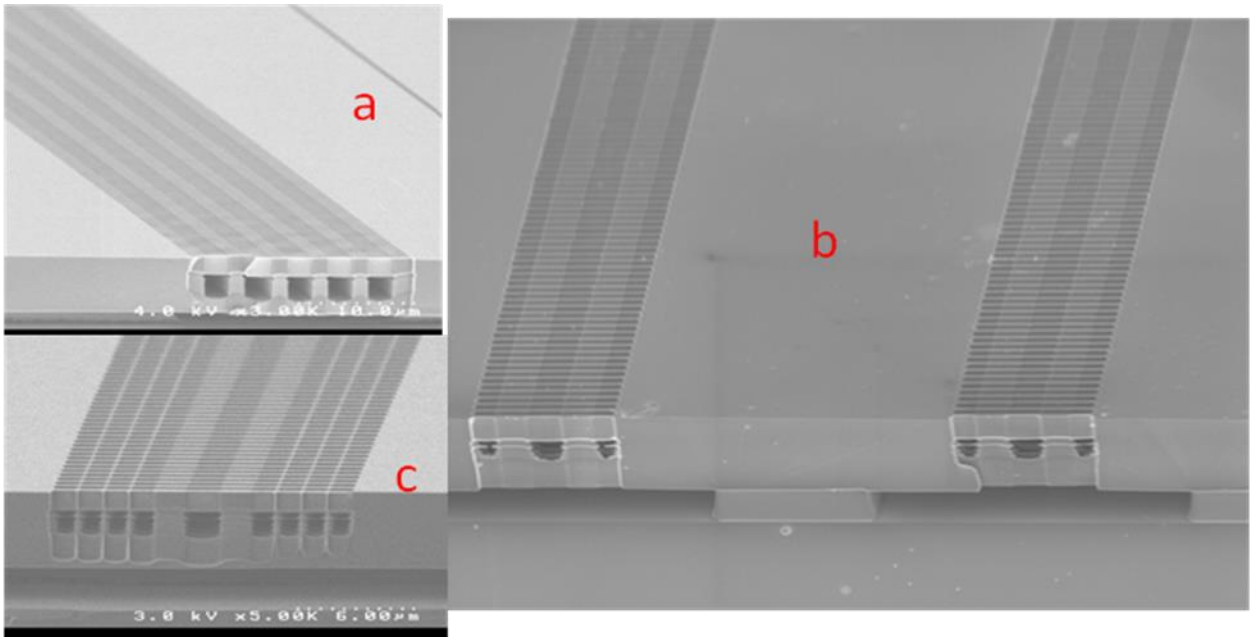

Fig. 2.6 SEM pictures of the metastructure cage waveguides of core size ~2 µm, HCG high 1.5 µm, period 627 nm in a) 5-waveguide array configuration; b) single waveguide supported by short arms; and c) single waveguide supported by long arms

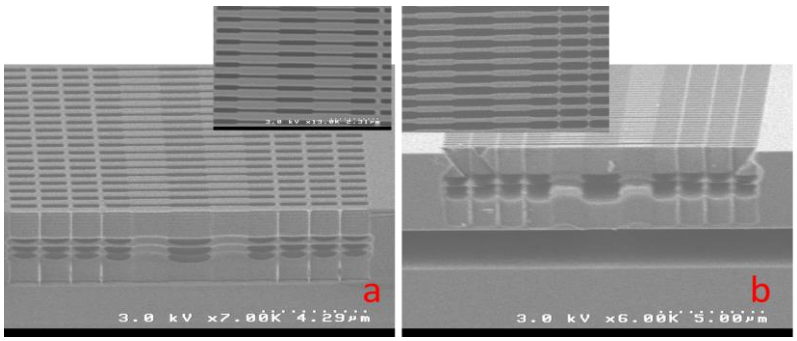

Fig. 2.7 The SEM pictures of the fabricated metastructure cage waveguide a) before and b) after the thermal oxidization and HF etching process

Previous work suggests that cryogenic ICP dry etch can produce smoother etching walls than that from Bosch etch.[10] Therefore, we attempted to develop a cryogenic etch to fabricated the waveguide structures. But, our initial results indicate that cryogenic etching is more difficult to control for very narrow, deep trenches. Therefore, we switched to the modified Bosch etch with the SCREAM method's isotropic undercut in an attempt to obtain smooth etch walls with the right HCG duty cycle.

The disadvantage of the modified SCREAM method is that the sample has to be taken out of the ICP machine after the first Bosch etch for PECVD SiO_2 deposit, then put back to the ICP machine for the second Bosch etch, perform the O_2 plasma etch, then the isotropic etch, and then the third Bosch etch. To avoid this multiple-stage etching process, we have attempted to use the same polymer deposit step in the Bosch etch instead the PECVD SiO_2 to put an additional coating on the top portion of the trench (top cladding/HCG region). The result, as shown in Fig. 2.7, shows that the isotropic etch in the core region started much quicker in the bottom than the trench wall, making the core region nonuniform again; therefore, we have to use the PECVD SiO_2 deposit for the modified SCREAM process. The advantage of the modified SCREAM process is that it does not produce the needle bars and reduces the roughness in the core region. More importantly, compared with the modified Bosch etch which can open the core region by undercutting only 50 to 100 nm maximum, the modified SCREAM method can expand the core region with no undercutting limit as long as the SiO_2 coating can hold. Therefore, we can use this method to produce a larger-scale waveguide structure, such as a terahertz waveguide.

2.4.3 Expansion for Terahertz Waveguide Fabrication

This type of artificial metastructure waveguide should be scalable for different operational wavelengths. As long as the index difference remains the same at the new wavelength and there is no significant absorption of the high index material, the waveguide propagation properties should be the same. We are developing the fabrication processes that can proportionally scale up our 1,550-nm operation waveguide to 1-THz operating frequency. For that, we are making a 3-D cage waveguide on a 800-μm Si wafer. We used the modified SCREAM etch method to fabricate an HCG cladding with a 100-μm period, 50% duty cycle, and 300-μm grating height from both the top and bottom surfaces of the wafer. The detail of this work will be presented elsewhere.

2.5 Experimental Test Results

2.5.1 Waveguide Guiding Test

Figure 2.8 shows the waveguide test setup and a picture of the waveguide output facet from the infrared (IR) camera. Strong guiding in our waveguides is observed from the IR camera. We used free-space microscope objective lenses to couple the laser light in and out of the waveguide sample that is mounted on an XYZ and tilt positioning mount. Two beam splitters are used to observe the input and out images with IR camera/monitors. To ensure that the incident laser beam is coupled into the hollow-core cage waveguide, we used free-space optics to align both a 1,550-nm tunable laser beam with a 632-nm HeNe laser on the same axis with the input focusing microscope objective lens. This allows us to view the input facet of the waveguide using a beam splitter and eyepiece lens, so we can ensure where the laser is focused into. The inserted IR camera image in Fig. 2.8 shows the guided waveguide output from an 11-mm-long cage waveguide sample. Each sample contains at least 10 identical waveguides that are separated by 20 μm. When we laterally move the sample to scan through the 10 waveguides, we can observe clearly that the light spot goes in a dim and bright cycle 10 times.

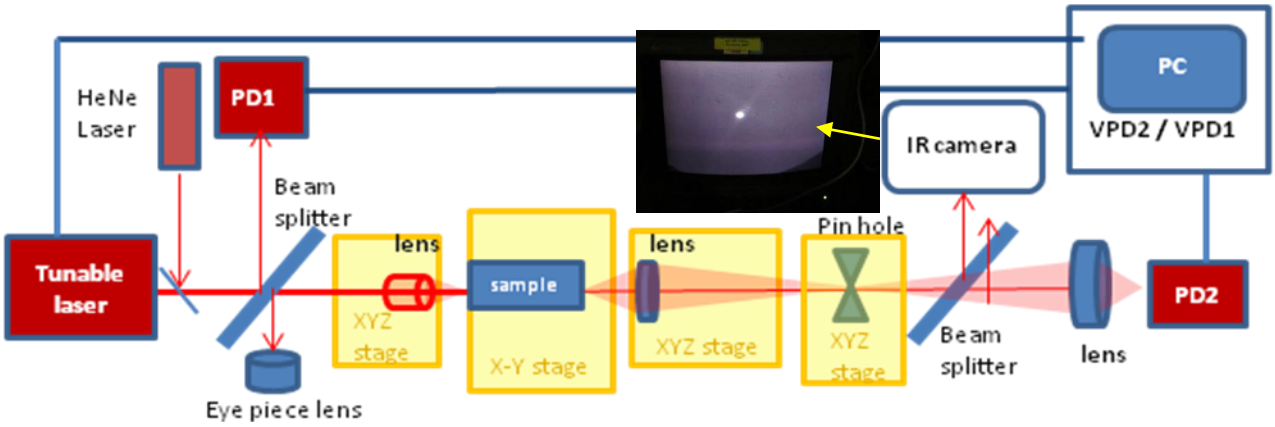

Fig. 2.8 Block diagram of the waveguide test setup

2.5.2 Waveguide Propagation Loss Measurement

Because of the nature of the hollow-core waveguide having no reflective facets and no core material scattering/absorption, only a cutback method can be used to determine the propagation loss of the waveguide, and our test setup is designed to accommodate this type of measurement. The measurement objective is to determine the waveguide's propagation loss as function of the wavelength. There are several challenges to our measurement: 1) the coupling loss may be an order

of magnitude larger than the propagation loss and may require many repeated measurements to reduce the error on the coupling loss by averaging; 2) there may be laser power fluctuation due to the wavelength tuning; and 3) interference from reflection surfaces of lenses and other optics in the measurement system may cause errors. Because of these factors, the standard deviation for this measurement can be as high as ±8 dB. To reduce the error bar, we have to increase the number of waveguides measured and average the results.

Figure 2.8 shows a schematic of the test setup used to measure propagation loss. We used an external-cavity laser, tunable between the wavelengths of 1535 and 1575 nm. We split the beam from the laser to a photodetector (PD) and into an objective lens. This objective lens is used to focus down the beam and couple it into the hollow core of the waveguide on the input facet. We installed another splitter before the input facet of the waveguide to split the beam to a PD (PD1) to monitor the input laser's intensity variation. Another objective lens is used to collect the light from the output side of the waveguide. We used an adjustable pinhole at the imaging plane of the second objective lens to cut out any scattered leakage light surrounding the guided beam. The beam is then split again to an IR camera for visual observation on a monitor and to a lens, which focuses the light to a second PD (PD2). The voltage reading from the first PD is used to normalize the voltage reading from the second PD as the laser is tuned across the wavelength range to generate a transmission curve. Transmission curves were then generated for the waveguide at different lengths. The measurement setup is not changed when obtaining transmission curves at different lengths except for mounting the sample and refocusing the 2 objective lenses for coupling and collecting the laser light into and out of the waveguide.

We have measured several waveguide samples. These waveguide samples were cleaved, and the transmission intensities were measured for multiple lengths of the waveguide as a function of optical wavelength. The waveguides are cleaved along an Si crystal plane to form the facets, and the waveguide lengths are measured under a high-power microscope. Each sample had 60 waveguides, and damaged ones were not included in the data sample. The cutback method is not ideal, as the waveguides can be damaged from excessive handling and cleaving, so extra care was taken for our measurements.

Figure 2.9 shows the transmission data for 16 identical waveguides on one of the samples at the lengths of 1.169, 0.867, and 0.475 cm. These waveguides have a core dimension of approximately 2 μm. The surface metagrating has a period of 625 nm defined in the fabrication process by ebeam lithography. The HCG high is about 1.5 μm. We attempted to fabricate waveguides with a 50/50 duty cycle, but because of the undercut etch required to form the hollow core, the duty cycle is

closer to a 35/75 (semiconductor/air) split. The transmission curve averages for the 3 lengths. From these, we then determined the waveguide loss per unit length from this set of data by taking the average value of loss between the normalized intensity measured from the different lengths, as shown in Fig. 2.10. There are a couple of low-loss regions, as shown at 1,547 and 1,557 nm, which indicate the loss could be less than 2 dB/cm. We have investigated our data and our measurement system. The small ripple in our data is attributed to the residue of the interference pattern in our measurement system that was not fully canceled by the normalization.

We have also measured a few other samples with different waveguide structure dimensions. The core sizes of these sample are D = 1 × 1 μm, 1.5 × 1 μm, 2 × 1.5 μm, and 2 × 2.5 μm. The initial length of the waveguides was 22 mm, which was cut back for various short lengths. The propagation losses of these waveguides are measured in the range of 1 to 5 dB/cm.

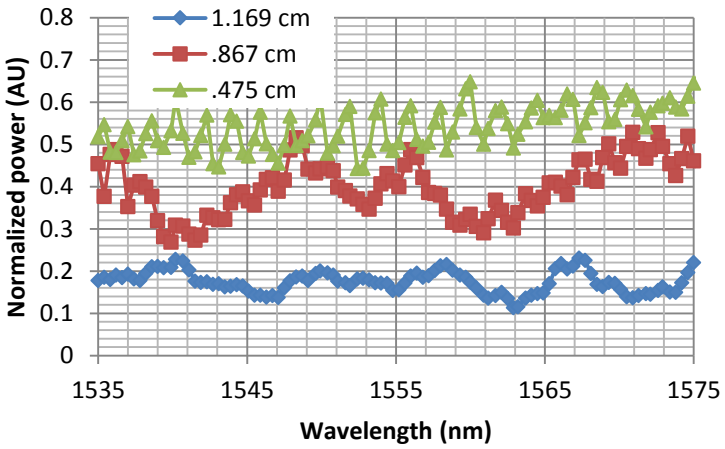

Fig. 2.9 Transmission curve averages of our waveguide for 3 different waveguide lengths

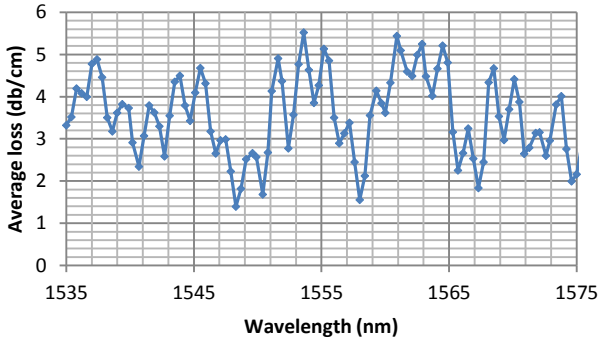

Fig. 2.10 Average propagation loss curve for our waveguide

2.5.3 Group Velocity Measurement

The group velocity was measured by sending a short optical pulse with pulse width on the order of 1 ns into the waveguide sample. As shown in Fig. 2.11, a wavelength tunable laser is coupled into an optical fiber, which is connected to a lithium niobate ($LiNbO_3$) Mach Zehnder modulator that is controlled by a function generator to create a short optical pulse with pulse width of 1.25 ns with less than 20% duty cycle. This pulsed optical signal is amplified by an Er-doped Fiber Amplifier and then focused into the waveguide's input facet via a tapered fiber-optical lens. A free-space microscope lens is used to focus the output facet image of the waveguide in a focal plane where a variable pinhole is introduced to block the leakage light and ensure that only the guided light from waveguide output passes. A beam splitter sends the image to an IR camera via its reflection path and sends the output signal to a 0.5-mm-diameter high-speed PD via a second lens in the transmission path. The PD's signal is sent to an oscilloscope channel, which is triggered by the pulsed signal directly sent from the function generator that is displayed by a second oscilloscope channel.

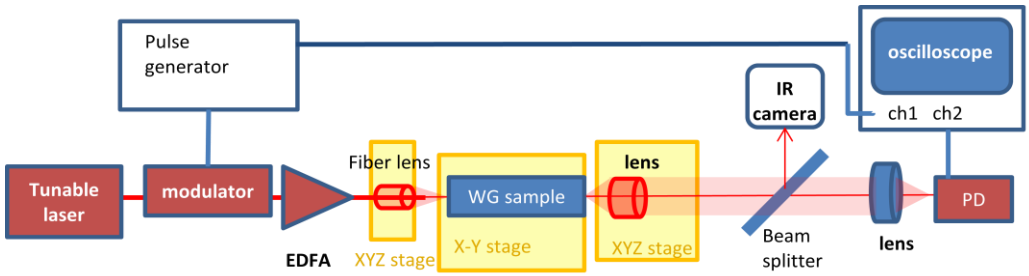

Fig. 2.11 Block diagram of the group velocity (waveguide delay) measurement setup

In order to determine the group velocity of the waveguide, we use the same experimental setup to repeat the experiment by just removing the waveguide sample and opening the pinhole to let the laser directly collected into the PD. Since the physical optical paths from the pulse light source to the PD for both experiments are the same, if the waveguide has a group velocity that is slower than the speed of light, we will observe a time delay at the oscilloscope. We have measured the transmission delay for several of our waveguide samples. Figure 2.12 shows the result of a pair of the optical pulses with and without the waveguide from the oscilloscope for one of these samples (sample 47) at the wavelength 1,530 nm. We observed an approximately 200-ps delay of the pulse transmitted through the waveguide with respect to the laser pulse propagating in the same path without the waveguide. The measured sample has its waveguide length cut at 16 mm. Therefore, we obtained a group velocity of approximately

21% speed of light, *C*. This is the same sample for which we measured the propagation loss, as shown in the last subsection of this report.

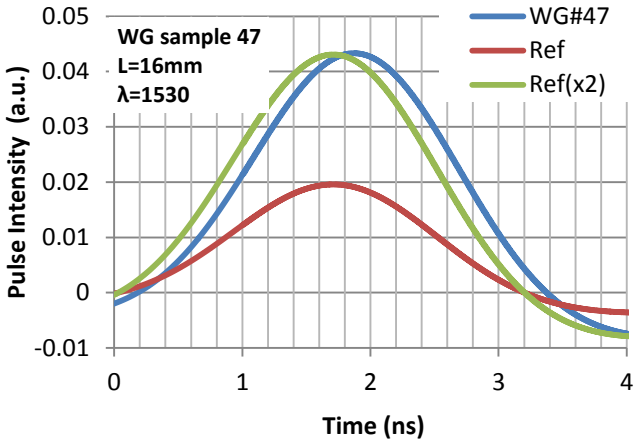

Fig. 2.12 Transmitted pulses from the oscilloscope with (blue) and without (red) the waveguide. For comparison, reference pulse intensity is multiplied by a factor of 2 (green) for normalization. Comparing the 2 pulse positions, there is a delay of about 200 ns of the pulse passing through the waveguide.

We also plot the delay time of the peak position as a function of laser wavelength from the waveguides in sample 47. Figure 2.13 shows these plots from one short-arm support waveguide, one long-arm support single waveguide, and the reference. We have measured other waveguide samples of different fabrication batches with slightly different structure dimensions. Using the physical length of these waveguide samples, we determined the group velocity of these waveguides to be in the range of 20%–30% of the speed of the light.

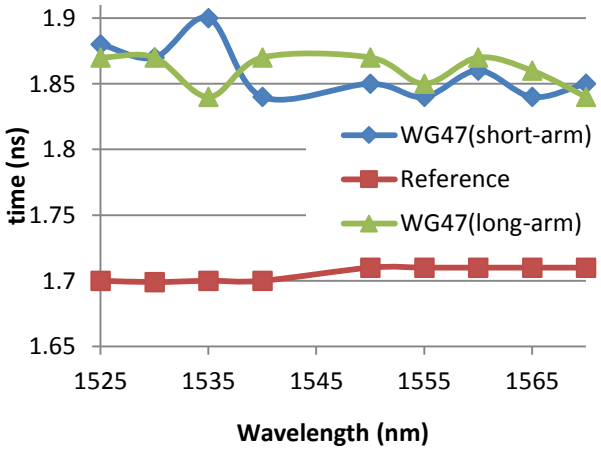

Fig. 2.13 Plot of the pulse peak position as a function of time for a pulse transmitted from a waveguide with short-arm support (blue), long-arm waveguide (green), and the reference pulse (red)

2.6 Discussion

The challenge is to obtain both slow-light and low-loss properties in the same operation bandwidth. The preliminary 2-D computation model indicates a bandwidth of 100 GHz of group velocity of 0.02c slow-light region with a 0.1 dB/cm low-loss. Our experimental results seem to be much worse than that model predicted. However, the preliminary modeling was made for a 2-D slab waveguide configuration formed by 2 infinitely large ideal HCGs; therefore, the results do not reflect our 3-D waveguide case. In the 3-D cage waveguide configuration, there must be "corner effects", and the polarization properties are also different compared with the 2-D case. We are developing 3-D simulation model codes to calculate the 3-D cage waveguide structure. Preliminary results do indicate a higher loss. In addition, this discrepancy could be attributed to a number of other factors:

- *Fabrication error*: From the SEM pictures, we can see that some of these samples still have the needle bars in the middle of the core region, and there is scalloping roughness on the vertical walls/posts, as well as a curved bottom grating shape.
- *Measurement error*: Since the insertion/coupling losses are an order of magnitude higher than the propagation loss, it is very difficult to repeat the exact coupling condition for each cleaves from sample to sample. There is also interference in our measurement system and unstable laser tuning that can increase the error in our measurement.
- *Wavelength*: We have a limited tuning range and tuning step accuracy for our laser. The wavelength or size discrepancy can occur between the calculated model and the real sample, which can put us outside of the optimum spot. Therefore, it is no surprise that we have not seen the desired slow-light/low-loss region from our first preliminary experiment. Either our laser tuning range could not reach the right wavelength or the fabrication errors are preventing the slow-light/low-loss region from being formed.

The preliminary calculation suggested that increasing the hollow core size *D* may reduce the propagation loss. However, reducing the hollow core size may reduce the group velocity. We aim to develop a better 3-D simulation model to calculate the exact 3-D cage waveguide structures in order to guide us in finding the optimum slow-light and low-loss spot. In the meantime, we are currently improving our fabrication tolerance/uniformity, fabricating and testing a large number of samples with slight variations in the metastructure period, duty cycle,

core size, grating width, etc., in order to reach a better slow-light/low-loss region experimentally.

2.7 Conclusion

We have demonstrated a new type of Si-based, high-contrast metastructure with a cage-like hollow-core waveguide that has both slow-light and low-loss properties. These 3-D metastructure cage waveguides were fabricated on an SOI wafer using our new nanofabrication techniques with the self-aligned modified Bosch etching process and modified SCREAM etching process. We experimentally demonstrated a group velocity of 0.2c slow-light waveguide propagation with about –2 dB/cm propagation loss. We continue to improve our fabrication process and our simulation model to reduce the loss and group velocity. This type of slow-light metawaveguide can provide a long time delay and high Q cavity in Si-based OEIC for chip-scale integrated photonics, RF-photonics, and systems for communication, radar, computation and sensor applications.

2.8 References

1. Mateus C, Huang M, Yunfei D, Neureuther A, Chang-Hasnain C. Ultra broadband mirror using low-index cladded subwavelength grating. IEEE Photonic Technology Let. February 2004;16(2):518–520.

2. Chang-Hasnain C. Zhou Y, Huang M, Chase C. High-contrast grating VCSELs. IEEE J Sel Top Quantum Electron. 2009;15(3):869–878, and Huang et al. A surface-emitting laser incorporating a high-index-contrast subwavelength grating. Nature Photonics. 2007;1:119.

3. Zhou Y, et al. Ultra-low loss hollow-core waveguides using high-contrast gratings. In: Proceedings of the Conference on Lasers and Electro-Optics/International Quantum Electronics Conference, 2009.

4. Zhou W, et al. Slow light high contrast metastructure hollow-core waveguides. Proc SPIE. 2012;8270:827009-1.

5. Sun T, et al. Low-loss slow light inside high contrast grating waveguide. Proc SPIE. 2012;8270:82700A-1.

6. Zhou W. Semiconductor hollow-core waveguide using photonic crystal gratings. United States patent US 8,506,829. 2013 Aug 13.

7. Laermer F, Schilp A. Method of anisotropically etching silicon. United States patent US 5,501,893. 1996 Mar 26.

8. Shaw KA, et al. SCREAM I: a single mask, single-crystal silicon process for microelectromechanical structures. In: MEMS '93. Proceedings of 1993 IEEE Micro Electro Mechanical Systems: An Investigation of Micro Structures, Sensors, Actuators, Machines and Systems; 1993 Feb 7–10; Fort Lauderdale, FL. New York (NY): IEEE. 1993; p. 155–160.

9. Soukoulis CM. The history and a review of the modeling and fabrication of photonic crystals. Nanotechnology 2002;13:420–423.

10. Taysing-Lara M, Dang G, Zhou W. A new fabrication method for 3D Si-based photonic crystal structure. Proc. of SPIE. 2011;7927:792707-1.

3. Design and Fabrication of 3-dimensional (3-D) High-Contrast Metastructure Terahertz Cage Waveguides

Gerard Dang, Monica Taysing-Lara, Weimin Zhou (SEDD)

3.1 Abstract

We have designed a new terahertz metastructure waveguide on Si wafers, aimed for low propagation loss and integration with Si-based integrated circuits (ICs). The waveguide has a round cross-section hollow core surrounded by a high-reflecting cladding wall, which is made by high-contrast metastructure gratings. We developed a new fabrication technique to fabric such a 3-dimensional (3-D) metastructure cage-like waveguide structure. The waveguide is built with an entire wafer thickness, which involves a deep silicon (Si) etch of periodically spaced holes and isotropic undercut etching to create a connecting circular hole in the middle of the wafer to form the waveguide's hollow core, then deep etch the high-contrast grating (HCG) through the whole wafer to form the cladding for the waveguide. We have successfully fabricated such a waveguide structure. The next step is to experimentally test and characterize the waveguide in the terahertz spectrum range.

3.2 Introduction

In recent years, there has been growing interest in terahertz research because of attractive applications, such as see-through imaging, chemical/biosensing and line-of-sight communications. However, terahertz technology is still in its infancy. Other than a few traditional optics, there is a lack of necessary devices and components to build circuitry to manipulate terahertz signals. To develop terahertz devices and components, the basic element is a terahertz waveguide. Using the traditional metal-tube microwave waveguide technology to build terahertz waveguides will result in high loss and high cost; plus, this traditional technology cannot be integrated with Si-based ICs.

Previously, we have developed a new type of 3-D cage-like high-contrast metastructure hollow-core waveguide that showed reasonable low-loss and slow-light effect at 1,550-nm operation wavelength.[1-3] It has been demonstrated that the high-contrast metastructure grating can be designed for very high reflectivity.[1] It then can be incorporated as the reflector in a hollow core waveguide without the use of metal. One of the potential applications for such a waveguide is in chemical gas sensing, because the cage design provides an open form of a high-*Q*

cavity that can be integrated with a light source and detector. However, it is desirable to perform the chemical sensing in the terahertz regime that has a less busy spectrum for easy chemical identification. Therefore, we have used the same design concepts to change the wavelength scale from infrared to terahertz to design a low-loss terahertz waveguide. We have developed a new fabrication technique to fabricate a terahertz metastructure cage waveguide on Si wafers.

3.3 Waveguide and Fabrication Designs

3.3.1 Waveguide Design and Simulation

Figure 3.1 illustrates a targeted cage-like high-contrast metastructure hollow-core terahertz waveguide structure to be constructed in an Si wafer. Since the electromagnetic wave at terahertz is in the order of 100 s μm in wavelength, we have to use the entire Si wafer thickness (~550 μm) to construct the waveguide. First, we worked with our collaborator at UC Berkeley to develop a theoretical computational model to simulate such a waveguide structure in order to guide us to design the hollow-core waveguide using the high-contrast metastructure gratings as waveguide cladding.

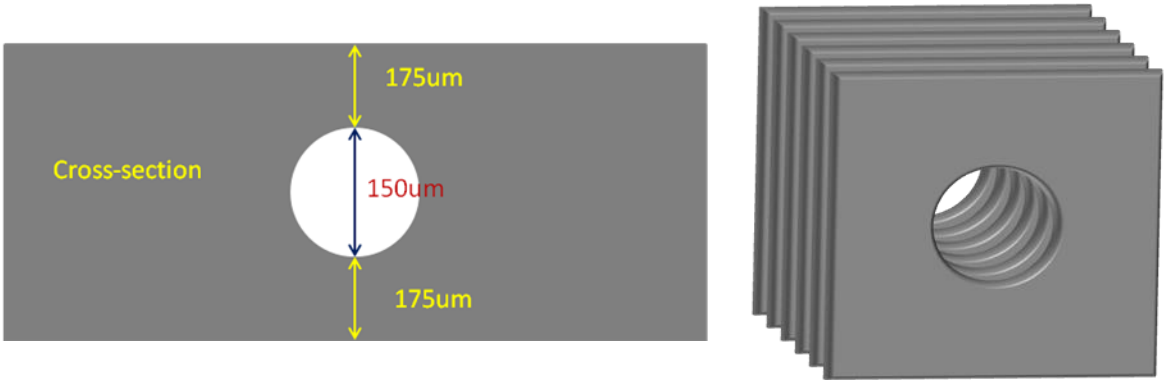

Fig. 3.1 Two- and three-dimensional cross-sectional diagrams of the terahertz hollow-core waveguide with high-contrast gratings. The axis for waveguiding is into the center of the cylindrical hollow core.

3.3.1.1. Dispersion Relation and Mode Pattern

To study the dispersion relation (i.e., $\omega\omega$-$\beta\beta$ diagram) of our 3-D waveguide, we use the dipole excitation method. In this method, dipoles with random orientation are put into the waveguide hollow core. Bloch boundary condition is set at 2 facets of one period. These dipoles will excite many modes inside the hollow core. After a long time decaying, only the intrinsic waveguide modes will build up a strong field and are shown to have strong field strength (shown as red color in Fig. 3.2a), and other lossy modes will decay out, leaving little intensity (shown

as white color in Fig. 3.2a). In this way we can study the dispersion relation inside our novel waveguide.

We simulated the dispersion relation for a waveguide with 2- × 2-μm core size, grating period 1 μm, duty cycle approximately 0.5, thickness for top/bottom grating 0.71 μm, and thickness for 2-side grating 1.77 μm. Dipoles excited modes with different frequencies and different wave vectors. When a stable state is reached, only the intrinsic mode will build up; this is shown as the red color in Fig. 3.2a. The black dashed line highlights the deep red region and indicates the mode dispersion curve. This mode is the intrinsic low loss mode supported by the structure. The black solid curve is the light line shown as general guidance. This particular waveguide supports the fundamental mode operation in the wavelength region we are interested in. The mode pattern for this fundamental mode is shown in Fig. 3.2b at a frequency of 1.698 THz, which is in the center of the fundamental mode band shown in Fig. 3.2a.

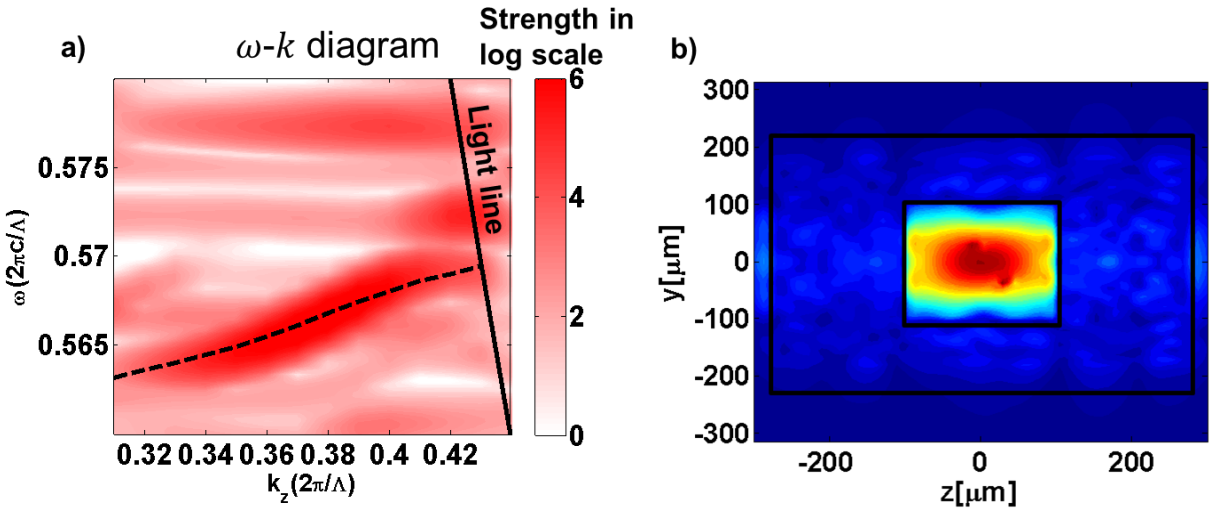

Fig. 3.2 a) Dispersion relation diagram of our 3-D waveguide. b) Mode pattern of the fundamental mode in our 3-D waveguide.

3.3.1.2. Intrinsic Propagation Loss

In this subsection, we will estimate the intrinsic loss of our hollow-core waveguide. An optical pulse centered at 1.698 THz with a 10-ps pulse is sent into the waveguide. The excitation and subsequent decay of the waveguide mode is sampled at various points inside the waveguide. The associated amplitude time signal is plotted in Fig. 3.3. We can see the source pulse at the very beginning and the slow decay of the intrinsic mode. Loss is then estimated following the formula

$$\text{loss}\left(\frac{\text{dB}}{\text{m}}\right) = 10 \times \log_{10} e \times s/v_g$$

where s is the slope of the decaying , and v_g is the group velocity of the mode. For the mode shown in Fig. 3.3, s is around 2×10^7/s and v_g is around 10^7 m/s. Thus, the estimated the intrinsic loss is around 8.6 dB/m. This loss can be further brought down by designing more reflective HCG as the waveguide walls.

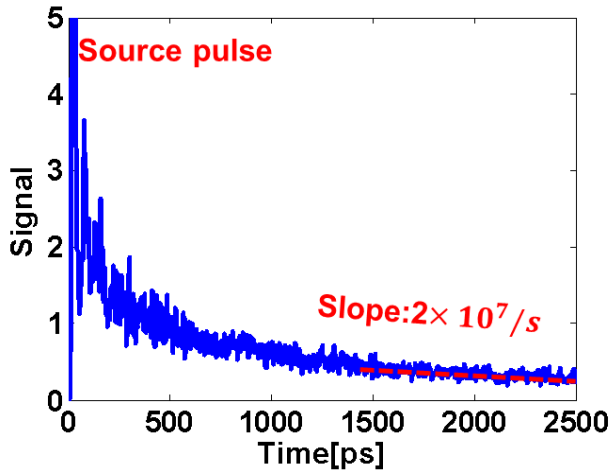

Fig. 3.3 The excitation of a 10-ps pulse and subsequent decay of the waveguide mode. Slope of the decaying is proportional to the waveguide loss.

3.3.2 Fabrication Technique

Unlike the near-IR hollow-core waveguides with HCGs we previously fabricated, e-beam lithography is not needed to fabricate these waveguides. The features are on the scale of tens of microns, and standard photolithography can be used. But, because of the large size of the waveguide core, we cannot use the same undercut etching method that we previously used for the near-IR hollow-core waveguide fabrication. To fabricate these terahertz waveguides, we need to develop a new undercut etch technique to create the 3-D cage-like structure that uses approximately 500 μm (entire wafer thickness) to construct the waveguide. As shown in Fig. 3.1, the waveguide core size is approximately 150 μm, leaving cladding dimensions of 175 μm. We used a modified "SCREAM" (Single-Crystal silicon REactive etch and Metal) process,[4] such as using a masking oxide on the surface of the wafer as well as on the sidewalls of etched trenches, but we also use chromium metal in addition to an oxide. We modified the process by using an inductively coupled plasma etching system, instead of a Reactive Ion Etcher, for our deep silicon etches. Also, instead of deposition of the oxide, we used wet thermo-oxidization of the Si to create the making layer.

We designed 2 photomask levels with grating patterns with a period of 100 μm and an approximately 50/50 duty cycle. As shown in Fig. 3.4, the first level of the mask design is used to access the center of the wafer to form the hollow core by

using a modified SCREAM process to undercut etch a column of connecting spherical holes to ultimately form a cylindrical hollow core for the waveguide. The second level is used to complete the formation of the high-contrast metastructure cladding in the waveguide via a deep Si etch through the entire thickness of the wafer.

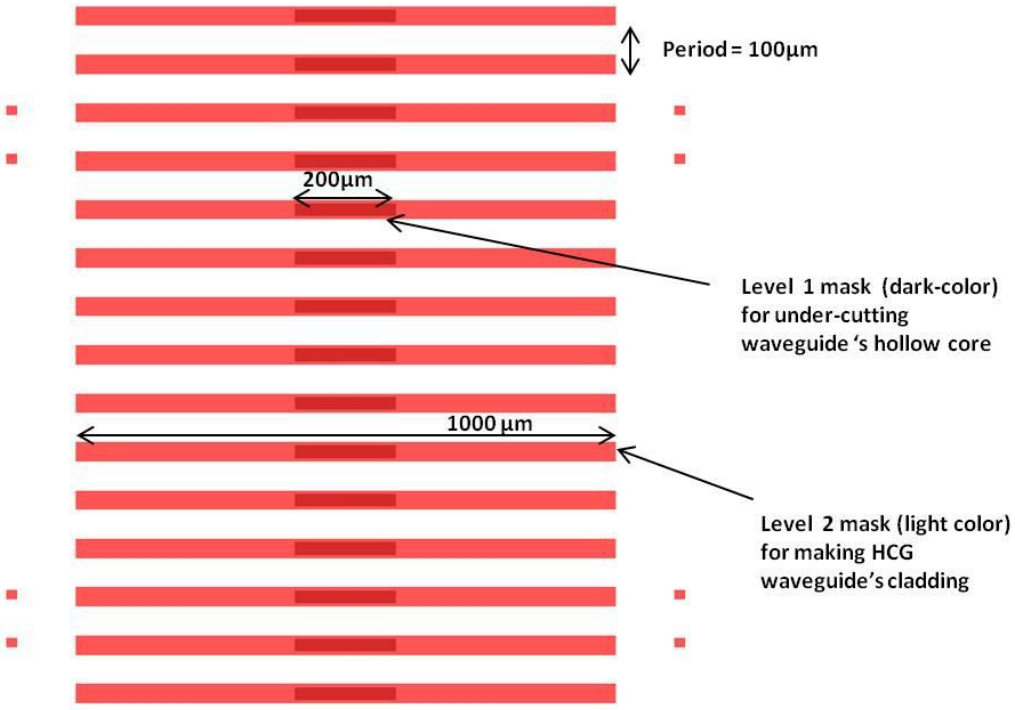

Fig. 3.4 Truncated .gds layout of overlaid mask levels. This would translate to a top view of the fabricated waveguide. The small boxes between the waveguides are alignment marks.

3.4 Fabrication

3.4.1 Undercutting Etch to Form the Waveguide Hollow Core

We are performing long-duration dry etches to form the features of the waveguide, so masking is important in the fabrication process. We start by growing a silicon dioxide (SiO_2) layer on the wafer using a wet thermo-oxidation furnace. The SiO_2 will be used as one way to protect the surface of the wafer during etching. The target thickness of the SiO_2 is 3 µm. Using AZ9260 photoresist spun-on and baked for a final photoresist thickness of 9 µm, we expose the photoresist with a pattern of the proper dimension for forming the core of the waveguide. The dark-colored rectangular boxes in Fig. 3.2 show the pattern used for this part of the process. These features after processing are about 50 × 200 µm in the Si. This mask level is used to etch down a series of deep trenches

about the height of the top grating (175 μm) to reach the top of the core area of the waveguide. These deep trenches provide access to the center of the wafer for the isotropic undercut etch for formation of a cylindrical core of the waveguide.

Following photolithography, the pattern is transferred to the SiO_2 layer by dry-etching the wafer using a CHF_3/CF_4 etch chemistry (Fig. 3.5). Standard Bosch etching is then used to etch approximately 200 μm of the Si wafer (Fig. 3.6). The Bosch etch[5] consists of 3 steps that are cycled to achieve deep etches in silicon while maintaining vertical sidewalls. The first step deposits a polymer conformally onto the trenches using a C_4F_8 plasma. Next, the polymer is anisotropically etched away at the bottom of the trench to expose the Si using a low-density SF_6 plasma.

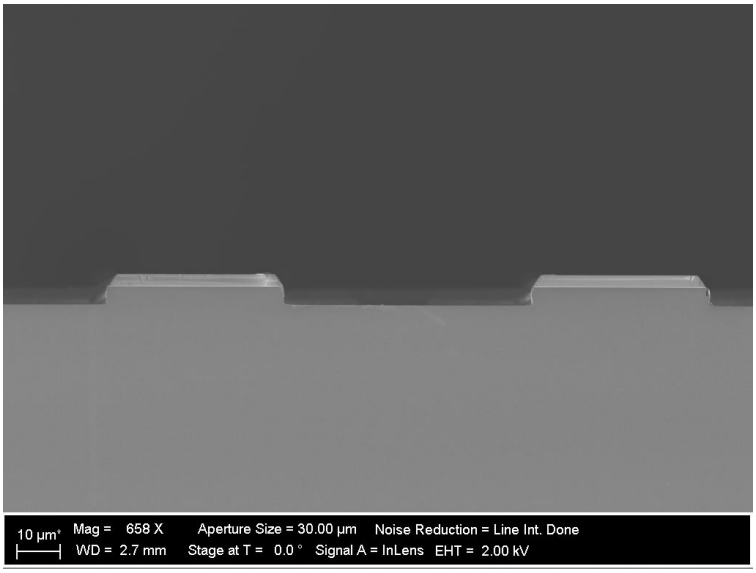

Fig. 3.5 Scanning electron microscope (SEM) image of wafer surface after the top-oxide etch. Dry-etching was used and some etching of the silicon occurred to ensure complete removal of the silicon dioxide. The photoresist mask was removed for the SEM image.

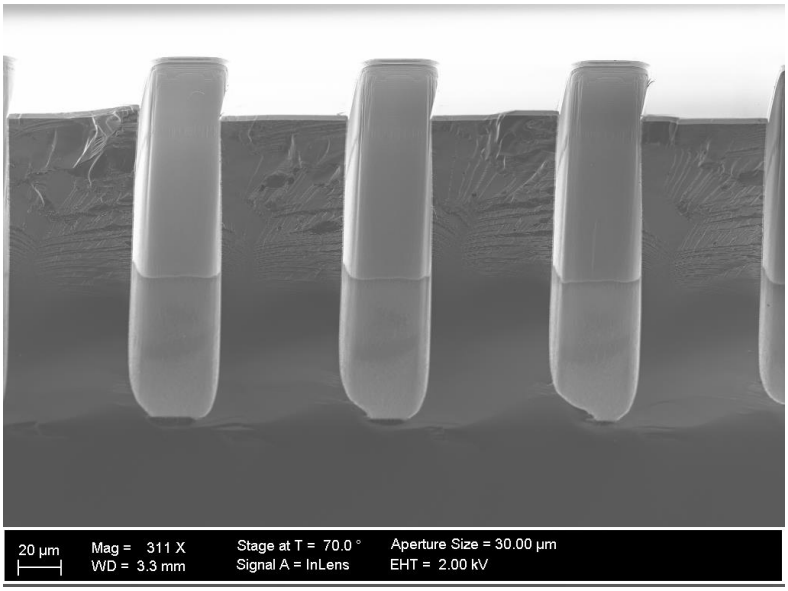

Fig. 3.6 SEM image showing the initial trench etch for reaching the center of the wafer prior to the hollow-core etch. A line can be seen in the trench because 2 separate Bosch etches were performed to achieve the desired depth.

Finally, the Si is etched away before etching can occur in the Si of the trench sidewall, as the polymer deposited on the sidewall is also being etched away during this step. The third step uses a high-density SF_6 plasma. This process is repeated to achieve a deep etch in Si with vertical sidewalls.

To prepare the wafer for the formation of the core, we want to protect the trench sidewall using SiO_2. We grow the oxide by again using a wet thermo-oxidation furnace, but because of the high temperature involved (1,100 °C), the photoresist on the wafer needs to be removed by acetone and the residual photoresist stripped using oxygen plasma. We then grow an approximately 5,500-A layer of the SiO_2 layer. To further protect the sidewall and the top surface, 3,000 A of chromium is deposited at a 45° deposition angle so that the metal is deposited only on the surface of the wafer and the upper sidewalls of the trenches, not in the bottom of the trench. We now have approximately 3.55 µm of SiO_2 and 3,000 A of chromium protecting the surface, and approximately 5500 A of SiO_2 protecting the trench sidewall. Chromium is not deposited at the bottom of the trench, but there is approximately 5,500 A of SiO_2 from the wet oxidation. We etch away the SiO_2 at the bottom of the trench using the same dry-etch process for SiO_2 used earlier and prepare the wafer for forming the core. The conditions for the undercut etch used to form the core are the same conditions as the third step of the Bosch process. This step etches Si isotropically. The profile of this etch in the Si is close to that of a sphere, and we target an etched sphere that has a diameter of 150–200 µm for a 500- to 550-µm-thick wafer. Because each trench etched into the Si

wafer is 50 μm away from an adjacent trench, the etched sphere punches through to form a cylindrical core along the length of the waveguide. Figure 3.7 shows a scanning electron microscope (SEM) image of the hollow-core etch. The surface of the sample used for this image shows damage from the scribe because a continuous cleaving plane in this direction does not exist in the Si after the hollow core is formed. So the waveguide's core is formed by the connecting spheres in the center of the Si wafer.

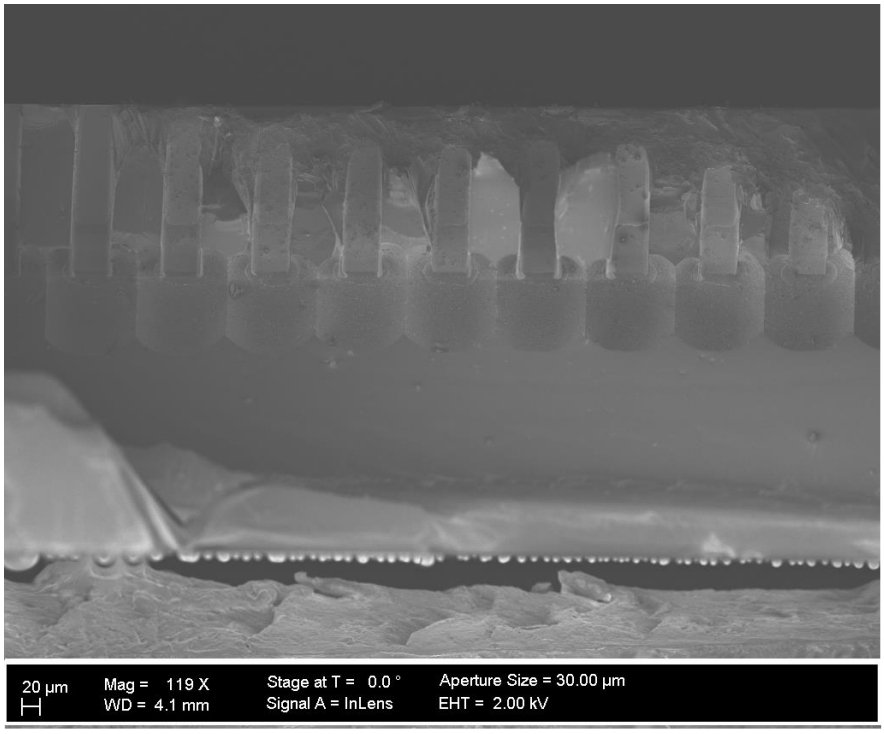

Fig. 3.7 SEM image showing the hollow-core etch in the wafer and the etched spheres punching through to adjacent spheres. The surface of the sample used for this image shows damage from the scribe because a continuous cleaving plane does not exist after the hollow core is formed.

3.4.2 Deep Through-Wafer Etch to Form the Waveguide's High-Contrast-Grating (HCG) Metastructure Cladding

Following the formation of the core, photolithography is performed again using a longer-lines feature to form the HCGs as the cladding of the waveguide. These are the longer grating features shown in the mask pattern in Fig. 3.4 that overlay the smaller rectangular features that were used for the under-cut etching of the core in the center of the waveguide. The dimensions of these grating bar features after processing are 50 μm × 1 mm. In order to etch into the Si using the wider grating feature, we must first etch through the chromium that was deposited earlier and the SiO_2 layer. The chromium is wet-etched using CR-9, which selectively etches

away the metal and not the SiO_2. The SiO_2 is then dry-etched using the same process as earlier. We then perform a Bosch etch through the entire thickness of the wafer to define the HCG claddings of the waveguide. Figure 3.8 shows a SEM image of the waveguide processed up to this point, viewing it in the direction of waveguiding.

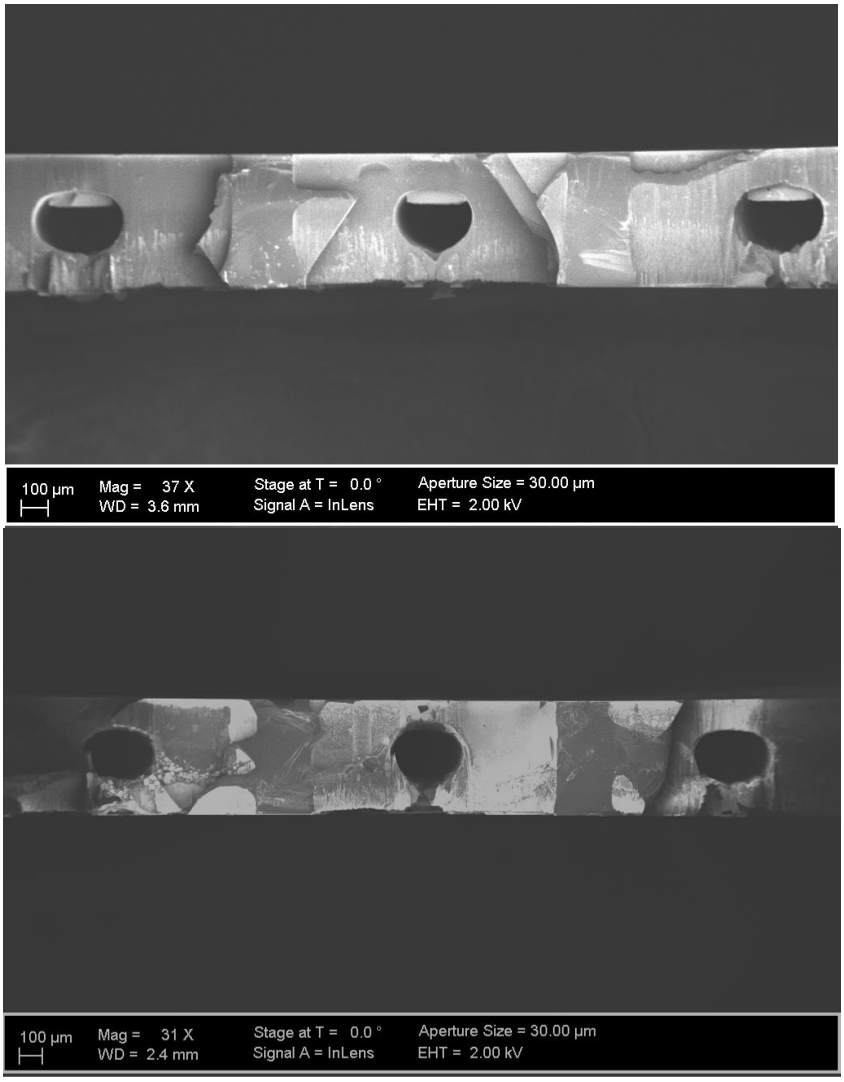

Fig. 3.8 Cross-sectional SEM images of the waveguides. (Top) An SiO_2 shell in the shape of the first trench etched can be seen at the top of the hollow core. (Bottom) The SiO_2 shell in the core was removed by buffered high-frequency etch.

The bottom corner of this facet is rough in the image because of scribing for preparing the SEM sample, but the bottom surface of the wafer is polished Si. The top SEM picture shows a shell of SiO_2 in the core of the waveguide. This was formed by wet oxidation in the trench sidewalls of the smaller grating feature used to access the center of the wafer prior to the hollow-core etch. The shell remains, as the Bosch process is highly selective to etching Si over SiO_2. We

remove any remaining SiO_2 on the waveguides by etching the wafer in buffered oxide etch as shown in the lower SEM picture. Figure 3.9 shows 2 SEM images of the completed waveguide.

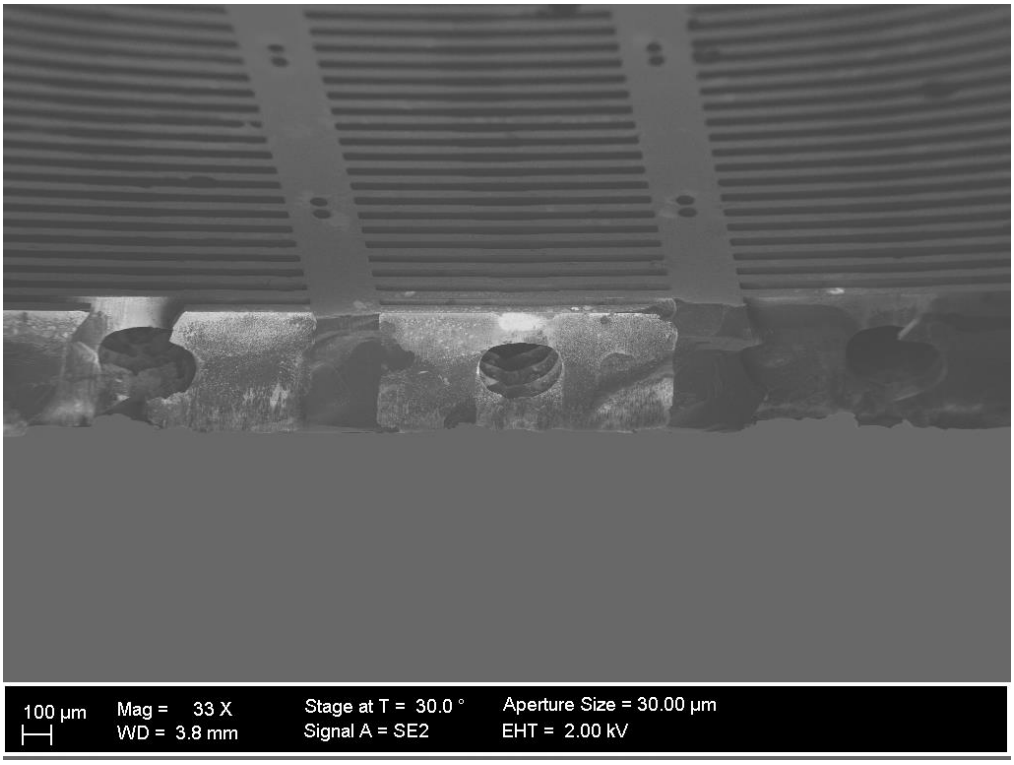

Fig. 3.9 SEM images of the waveguides after etching in CR-9 and buffered oxide etchant

3.5 Conclusion

We have designed and fabricated new terahertz high-contrast metastructure cage hollow-core waveguides. These 3-D metastructure cage waveguides were fabricated on standard 4-inch Si wafers with a thickness of approximately 550 µm using modified SCREAM and Bosch etch processes. We are continuing to improve our fabrication process and are preparing the waveguides for testing and measuring propagation loss. This type of waveguide can potentially be used as a basic building component in circuitry designed to manipulate terahertz signals as well as a chemical-biological sensor because of its open-cage design.

3.6 References

1. Zhou Y, et al. Ultra-low loss hollow-core waveguides using high-contrast gratings. In: Proceedings of the Conference on Lasers and Electro-Optics/International Quantum Electronics Conference, 2009.

2. Zhou W. Semiconductor hollow-core waveguide using photonic crystal gratings. United States patent US 8,506,829. 2013 Aug 13.

3. Zhou W, Dang G, Taysing-Lara M. Demonstration of a slow-light high-contrast metastructure cage waveguide. Proc. of SPIE Vol. 8633; High Contrast Metastructures II; 2013 Mar 15. 863305.

4. Shaw KA, et al. SCREAM I: a single mask, single-crystal silicon process for microelectromechanical structures. In: MEMS '93. Proceedings of 1993 IEEE Micro Electro Mechanical Systems: An Investigation of Micro Structures, Sensors, Actuators, Machines and Systems; 1993 Feb 7–10; Fort Lauderdale, FL. New York (NY): IEEE. 1993; p. 155–160.

5. Laermer F, Schilp A. Method of anisotropically etching silicon. US Patent No. 5501 893.

4. Tunable Terahertz Metamaterial Devices

Monica Taysing-Lara, Gerard Dang, Grace Metcalfe, Nathaniel Woodward, Weimin Zhou (EO&P, SEDD)

Daniel Shreiber, Eric Ngo, Matt Ivill, Melanie Cole (M&MS, WMRD)

Amir Zaghloul (E&RF, SEDD)

4.1 Abstract

We have designed several tunable terahertz metamaterial structures containing 3-dimensional (3-D) metal split-rings with a tunable capacitor fabricated using complex oxide thin films (in this case, BaSrTiO3 [BST]). Subsequently, the team developed a new fabrication technique and successfully fabricated such a 3-D tunable metamaterial device. In addition, a simulation model was developed to assist the metamaterial device design and predict the resonance frequency and tuning. The model has also been used to determine the dielectric constant of the BST thin film and to assist in BST thin film tunability measurements. This is, to our knowledge, the first effort to measure the BST thin film tunability in the terahertz spectrum.

The free space evaluation of the metamaterial device in the terahertz spectrum has been performed and is in general agreement with the stated goals of this DSI: a fabrication of a tunable metamaterial device in the terahertz spectrum.

4.2 Introduction

Metamaterial is a man-made material that has some engineering-designed electromagnetic properties, such as specific ε and μ in a desired frequency bandwidth. In order to obtain a desired value for ε and μ (in particular, the negative values for ε and μ are of special interest), one has to manipulate or create certain energy state "transitions". That can be done by creating a group of micro-resonators as unit cells in the metamaterial, such as metal split-ring resonators. In this project, our objective is to develop a tunable metamaterial device in the terahertz operation band. There are many interesting terahertz system applications for the Army, such as see-through imaging, chemical/biosensing, and line-of-sight communications. However, terahertz technology is still in its infancy. There is a lack of necessary devices and components to build circuitry to manipulate terahertz signals. To develop terahertz devices and components, the traditional materials often have inadequate electromagnetic properties that result in loss or unresponsiveness if used to build a terahertz device. Metamaterial may offer new

opportunities for solving this problem, and tunable metamaterial may provide even more freedom for design of such a terahertz device. The most desirable electromagnetic property for such a metamaterial is to have the value of ε and μ to be able to tune over a certain terahertz frequency range, to have a tunable resonance, or have the so-called double negative ε and μ so that special optical properties can be realized. However, this will require a special 3-D geometric topology for the split-ring unit cells; the traditional semiconductor device fabrication processing technique may not be able to realize such device geometry. In this project, we developed a new fabrication technique which allows us to build a specific 3-D split-ring structure that realizes the desired device's geometric configuration. The goal of this project was to achieve the first step: to fabricate a single negative tunable terahertz metamaterial device into a configuration that will enable easy transformation into a double-negative device.

4.3 Design, Modeling, and Simulation

The DSI team worked together to design 8 versions of the tunable terahertz metamaterials. Two of them that contain 3-D metal split-rings with tunable capacitance fabricated using complex oxide (BST) thin films were down-selected. Figure 4.1a shows the unit cell of the metamaterial device. A tunable capacitor is formed in the gap of the metal split-ring. A complex oxide (BST) thin film is used as the dielectric media for the capacitor because BST has a very high dielectric constant in the high-frequency band. The BST thin film on top of a substrate (sapphire) is sandwiched between 2 metal electric strip lines that are perpendicular to the surface of the split-ring. A direct-current (DC) bias can be applied to these electrodes to tune the capacitance in between the metal split-ring. The standing-up metal split-ring is wrapped around on the surface of a rectangular polymide ridge bar, which is formed on top of the substrate and BST film. Figure 4.1b shows the split-ring arrays with the DC metal bias electrodes that can apply bias to all the capacitors in the gaps of the split-rings.

The Weapons and Materials Research Directorate (WMRD) team led the simulation work of the metamaterial and the thin-film growth development of the Ba1-xSrxTiO3 (BST) as the tunable capacitor material. A commercially available high-frequency structural simulator (HFSS) software that solves Maxwell equations for the waves propagating in the materials of interest has been used to develop the model for the simulation. Figure 4.2 shows simulation results, indicating that in addition to the resonant peak, interesting effects of nonresonant energy dissipation of the impinging wave at certain frequencies can be seen as a result of the interference-like behavior.

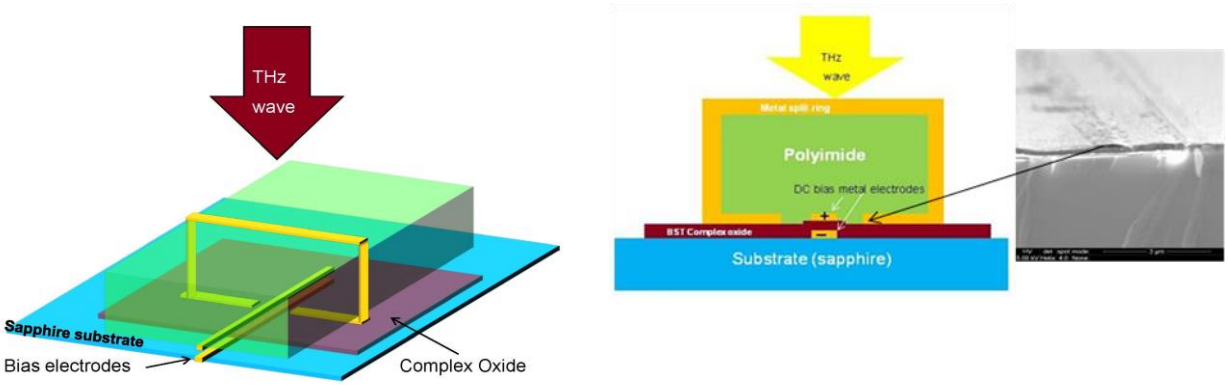

Fig. 4.1a Tunable 3-D terahertz metamaterial unit cell. (Left) Cross section of the split-ring unit cell with complex oxide film as tunable capacitor (right) and (right inset) scanning electron microscopy (SEM) picture.

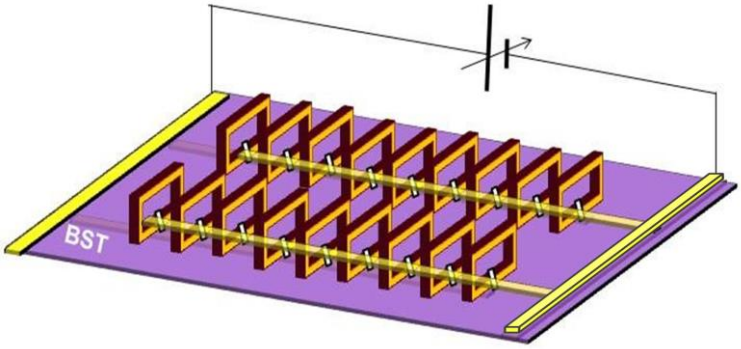

Fig. 4.1b 3-D illustration of the tunable metamaterial

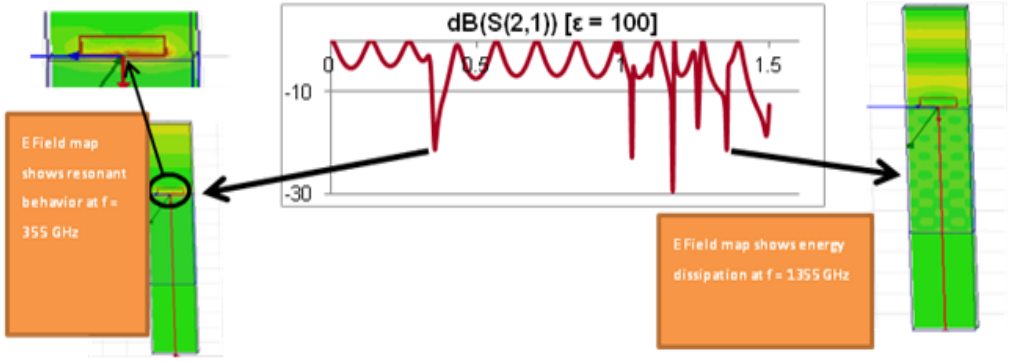

Fig. 4.2 HFSS model simulation of the test surfaces showing the resonant frequency and some nonresonant energy dissipation

In the Sensors and Electron Devices Directorate (SEDD), we developed a method of measuring and analyzing the complex refractive index of a variety of thin films, as well as substrate material, using differential time-domain terahertz spectroscopy (TDTS) in the 0.1- to 2-THz range (Fig. 4.3).

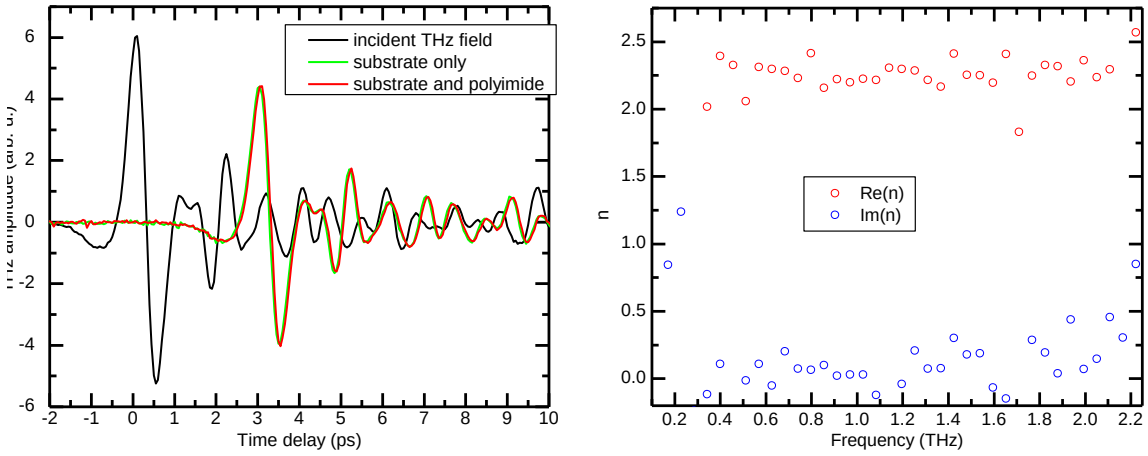

Fig. 4.3 (Left) Time-resolved terahertz transmission spectroscopy data and (right) complex refractive index of a polyimide thin film on sapphire

The experimentally measured indices are used in the simulation model, which predicts the resonant frequency of the metamaterial. For example, a shift of 0.11 THz occurred when the dielectric constant of the BST was increased from 100 to 500. Using the differential TDTS system, we measured the refractive index of the substrate material's sapphire as $n = 3.06 \pm i0.01$ and silicon as $n = 3.52 \pm i0.02$ in the terahertz frequency range. For thin films, we measured $n = 2.25 \pm i0.04$ for a 9.54-μm-thick polymide film on a sapphire substrate. As seen in Fig. 4.1, the polymide is part of the 3-D metamaterial structure.

The model has been devised to predict the resonance response of the designed metamaterial surface when the dielectric constant of the BST thin film is known or, alternatively, the model can determine the dielectric constant of the BST film by comparison with the experimental data (Fig. 4.4).

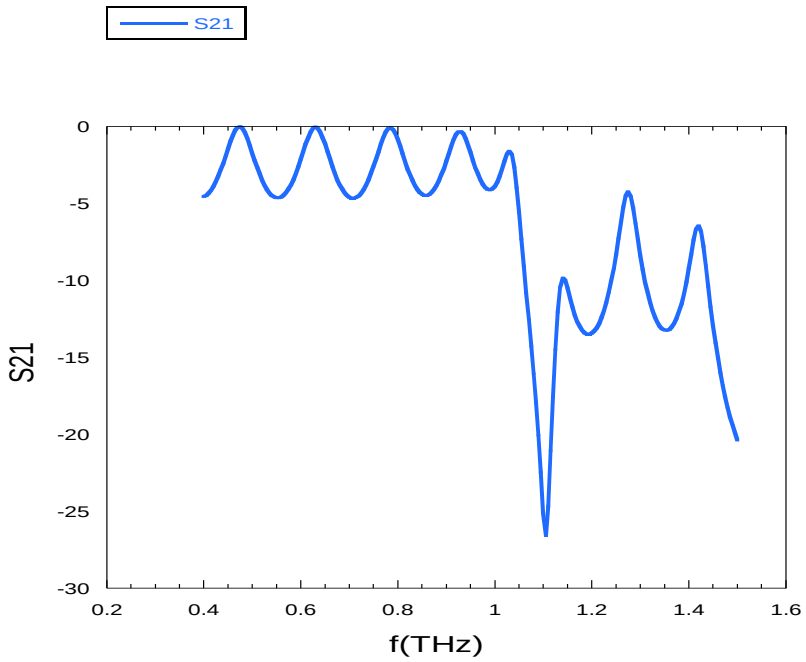

Fig. 4.4 Results from the HFSS model of the designed and implemented metamaterial surface. The location of the resonance peak is accurately predicted with assumed value of BST dielectric constant.

Hence, the model can be applied to find the change in dielectric constant from the resonance peak shift when the DC voltage bias is applied. Figure 4.5 shows the simulated resonance shift of 1 GHz when the dielectric constant of BST is increased from 170 to 180. This is the first time the tunability of BST in the terahertz regime has been measured as a function of bias in the metamaterial device. The experimental results of the resonant frequency shift by 2 GHz (when 6 V is applied) were compared with the confirmed model that showed a 1-GHz leftward shift of the resonant frequency peak when the dielectric constant of BST is increased from 170 to 180.

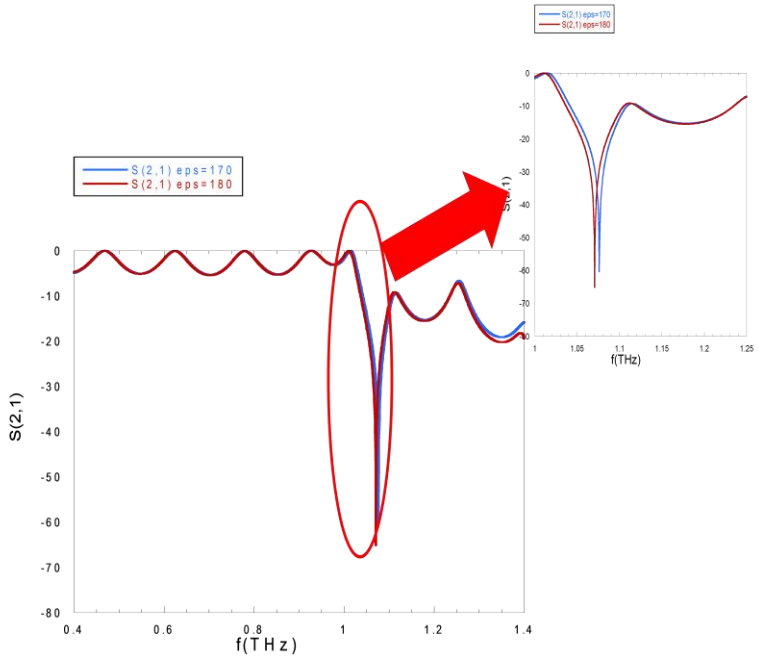

Fig. 4.5 HFSS model of the metamaterial device when BST thin film is assumed to have a dielectric constant of 170 (blue) and 180 (red). The 1-GHz leftward shift is analogues to the 4-V bias applied to the device (experimental data).

4.4 Fabrication

4.4.1 Develop Fabrication Technique

Led by SEDD, we developed a new fabrication technique for the tunable split ring resonators. The fabrication consists of a bottom bias electrode metal on a sapphire substrate, the BST layer, a top bias electrode metal, and a 5,000-Å copper deposition for the bottom of the split-ring. Then a 10-μm polyimide rib structure is built.

4.4.2 BST Thin Film Growth

A 180-nm-thick BST film was grown and characterized both at SEDD and WMRD. The thin film was grown at an ambient temperature of 490 °C, base pressure of 5 × 10^–8 Torr, and deposition pressure of 10 mTorr. The deposition gas mixture was 90%Ar/10% O2. The deposition time was 4 h 15 min at radio frequency (RF) power of 150 W. Figure 4.6 shows one of the BST thin films grown at WMRD. Although the BST film was too thin to measure the complex refractive index accurately, the refractive index can still be deduced by measuring the metamaterial resonance frequency with the help of the devised model.

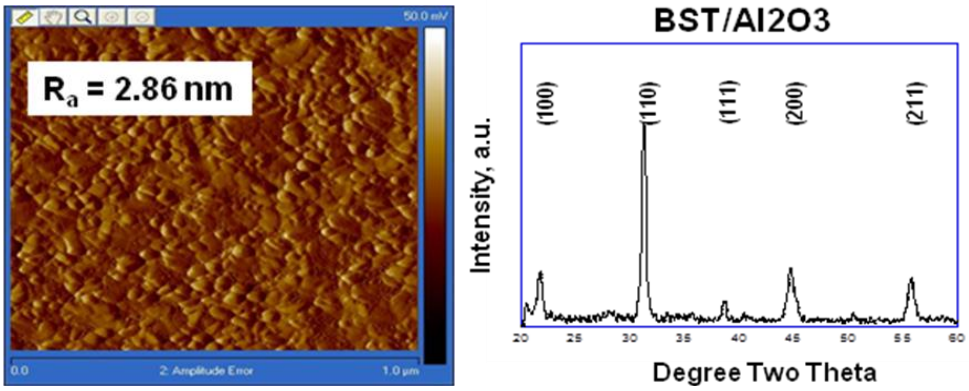

Fig. 4.6 (Left) Atomic Force Microscopy (AFM) image and (right) X-ray diffraction (XRD) image of BST thin film grown on sapphire substrate

4.4.3 Bias metal lines

Two DC metal bias electrode lines are deposited below and above the BST thin film to form the tunable capacitors in between the gap of the split-ring (Fig. 4.7). We first used photolithography with our first-level mask and platinum (Pt) metal evaporation process to deposit the bottom electrode lines on the sapphire substrate. Pt metal can survive the high-temperature growth process of the BST thin film on top of these metaelectrodes. Once the BST film is grown, we use photolithography again to deposit the top DC electrode and the bottom portion of the metal split-rings. After the lithography, 200 Å of titanium and 5000 Å of copper were evaporated using a CHA ebeam evaporator; then a sample was immersed on acetone for 30 min and put under the ultrasonic for 30 s for metal liftoff.

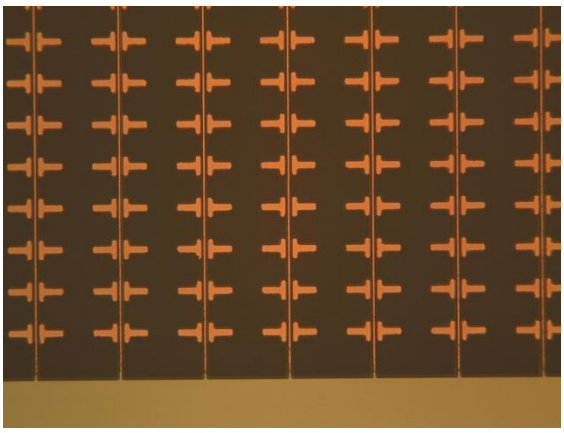

Fig. 4.7 Top and bottom electrode

4.4.4 3-D Split-Ring Fabrication

To create the standing metal split-rings, we need to first form an array of polyimide rectangle ridge bars that have a cross-section size that matched the split-ring size, which is about 10 μm high and 50 μm wide. The center of these ridge bars was aligned on top of the bottom portion of the split-ring that is already deposited on the substrate with the tunable capacitors that were made in previous steps. A third-level mask is used to create these polyimide bars by lithography and high-temperature curing as follows: Polyimide HD 4100 was poured using a dropper and let sit for 5 min; air bubbles at the top were removed with the dropper. Then the sample was spun at 1,500 rpm for 40 s and soft-baked at furnace for 10 min at 95 °C. Poly Mask was used to expose the polyimide for 15 s using 300 W and post-expose-baked at the furnace at 95 °C for 50 s. The polyimide was developed by immersing the sample on the PA 401 solution for 2 min and rinsing on the PA 400 solution for 30 s; after that, it was blow-dried with the air gun. Finally, the sample was hard-baked at the furnace under oxygen, and the temperature was increased at a rate of 10 °C/min until 200 °C then baked for 30 min, then increased at the same rate to a temperature of 375 °C and baked for 60 min. The polyimide scum from the top of the metal was removed by using the Metroline/IC Plasma using 200 sccm of oxygen and the power of 200 mW at the pressure of 1 Torr for 10 min. The polyimide thickness, 9.8 μm, was obtained using a SEM.

Once the polyimide bars are made, we spin a thick photoresist on top of it. Using the fourth-level mask lithography, we open a line slot on the photoresist that is across the top of the polyimide bar so that a series of lines on the top and side of the polyimide are exposed. The next step is to evaporate metal by tilting and rotating the wafer 45° to the evaporation source. Then, 200 Å of titanium and 5,000 Å of copper were deposited using a CVC 610 sputtering system. The sample was immersed in acetone for 30 min and put under the ultrasonic for 30 s for metal liftoff. The result is that a series of half metal rings are wrapped around the polyimide bars. The first fabricated metamaterial device is shown in Fig. 4.8.

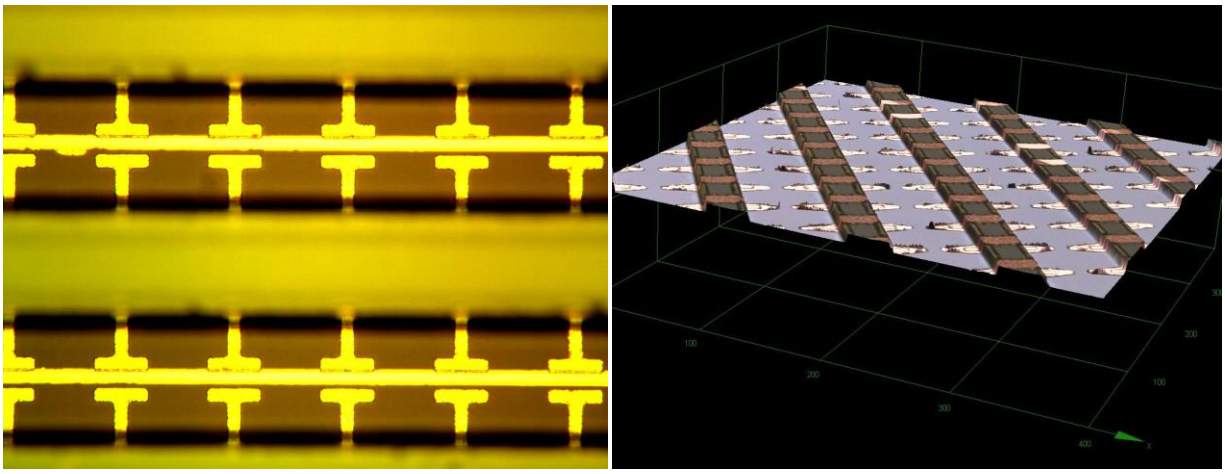

Fig. 4.8 Left: microscope picture of the split-ring arrays focused on the bottom tunable capacitor with metal contact line; Right: 3-D optical microscope picture of the split-ring metamaterial device

4.4.5 Device Characterization and Test

Polarization-dependent terahertz transmission experiments were conducted to determine the resonant behavior of the structures with and without the BST layer as shown in Fig. 4.9. For each sample we compare transmission of terahertz radiation parallel and perpendicular to the split ring relative to the terahertz transmission through the air. The overall absorption through the devices due to the BST layer, copper contacts, and substrate can be seen when the incident terahertz is polarized perpendicular to the split-ring resonators (SRRs), where we do not expect to see resonant behavior. When the incident terahertz is polarized parallel to the SRRs, the sample containing a layer of BST shows a strong broad absorption in the 1–2 THz region, while the sample without BST contains a sharper absorption around 1.75 THz.

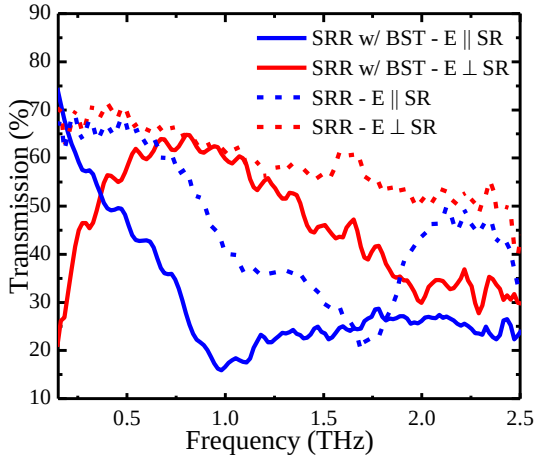

Fig. 4.9 Polarized terahertz transmission through SRR structures

We have characterized the first designed and fabricated active metamaterial with time domain terahertz spectrometer (Figs. 4.10 and 4.11) for tunability.

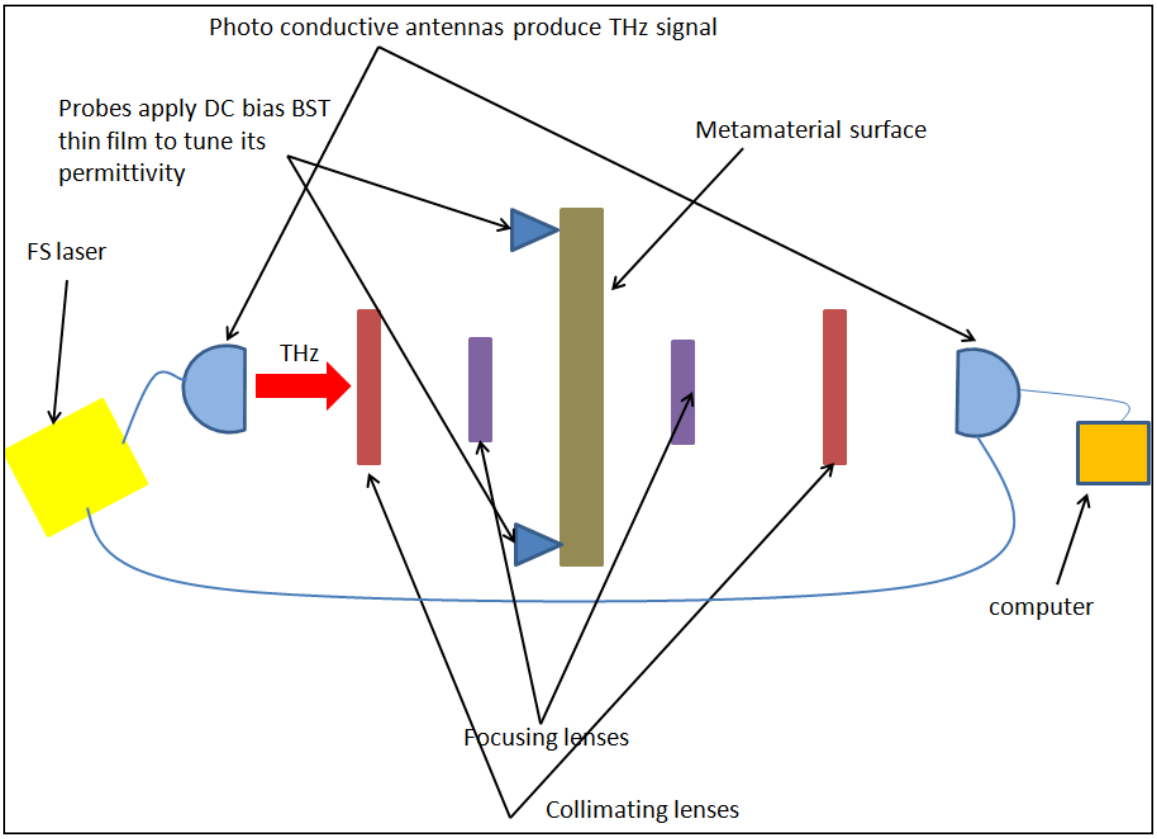

Fig. 4.10 Schematics of the experimental setup for WMRD's terahertz time-domain spectrometer

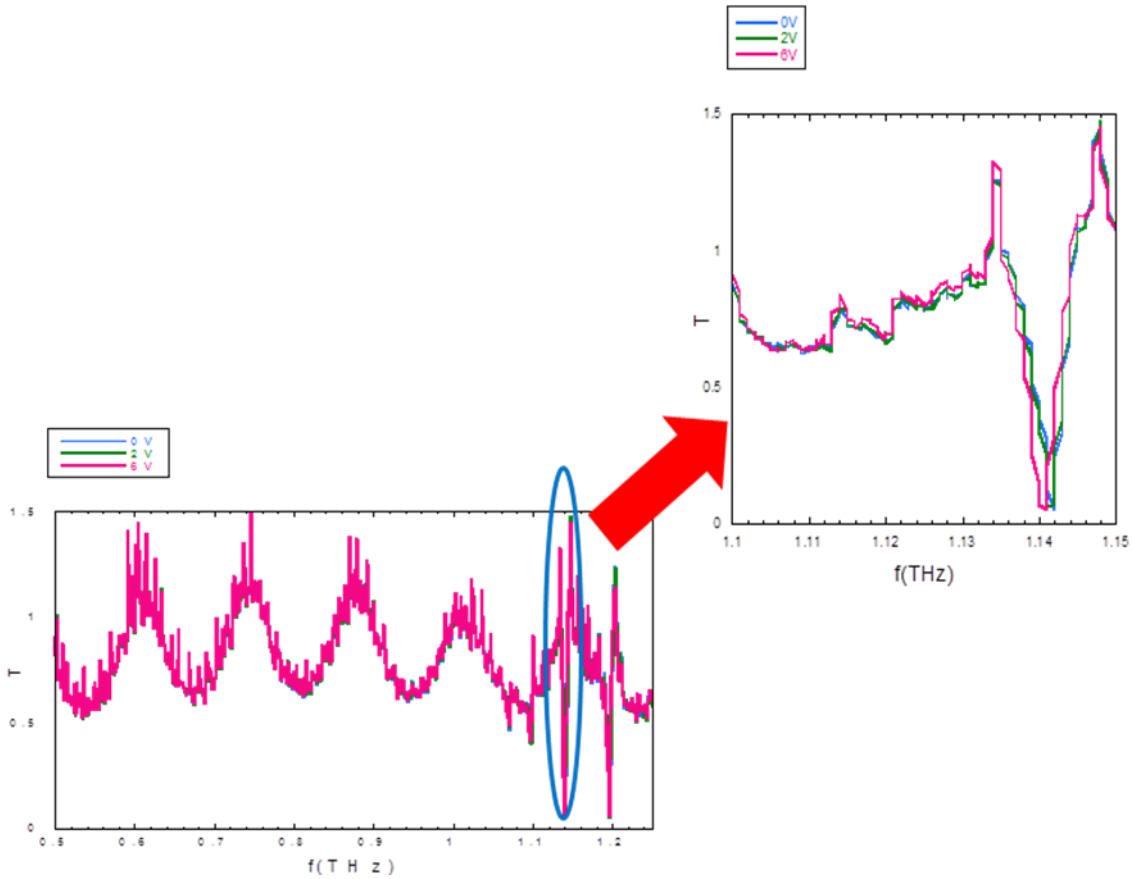

Fig. 4.11 Resonant peak shift when the bias of 0, 2, and 6 V is applied to active metamaterial in time-domain terahertz spectrometer. The inset shows a 2-GHz shift in resonance frequency when a 6-V bias is applied.

Bias applied to the BST thin film (up to 6 V) had shifted the resonant peak of the device by 2 GHz (from 1.142 to 1.14 THz) as indicated in the inset of Fig. 4.11.

The shift is quite remarkable since because of an insufficient thickness of the bottom bias electrode, only a small portion of the "capacitor gap" is filled with BST thin film (Fig. 4.12) and, hence, the fields that interact with the BST film are much lower than the theoretical capability of the device.

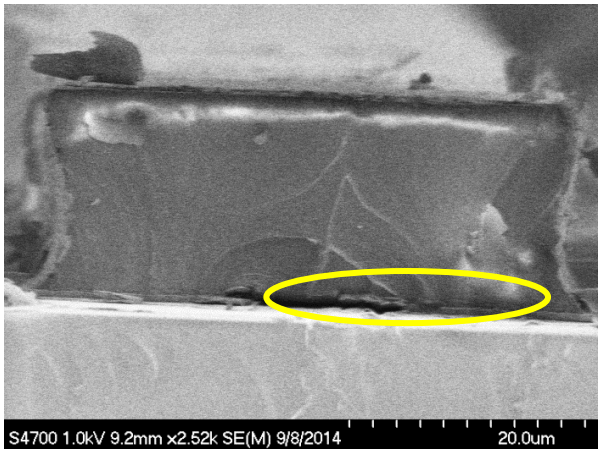

Fig. 4.12 SEM of THz metamaterial unit cell with unfilled "capacitor gap". The schematics of the structure are provided in Fig. 4.1.

4.6 Terahertz Transparent Electrode Study

The efficiency of the metamaterial device can be further enhanced by using DC bias electrodes composed of a DC conductor that is transparent to terahertz radiation, e.g., indium tin oxide (ITO). ITO films were grown with varied ambient argon (Ar)/oxygen (O_2) ratios at WMRD and characterized at SEDD for transparency in the terahertz regime (Fig. 4.13). We found the correct ratios to produce the terahertz transparent ITO films with 2 orders of magnitude higher resistivity with respect to the nontransparent ITO. The terahertz transparent electrodes grown under the devised conditions can be used in future terahertz metamaterial devices to enhance their efficiency.

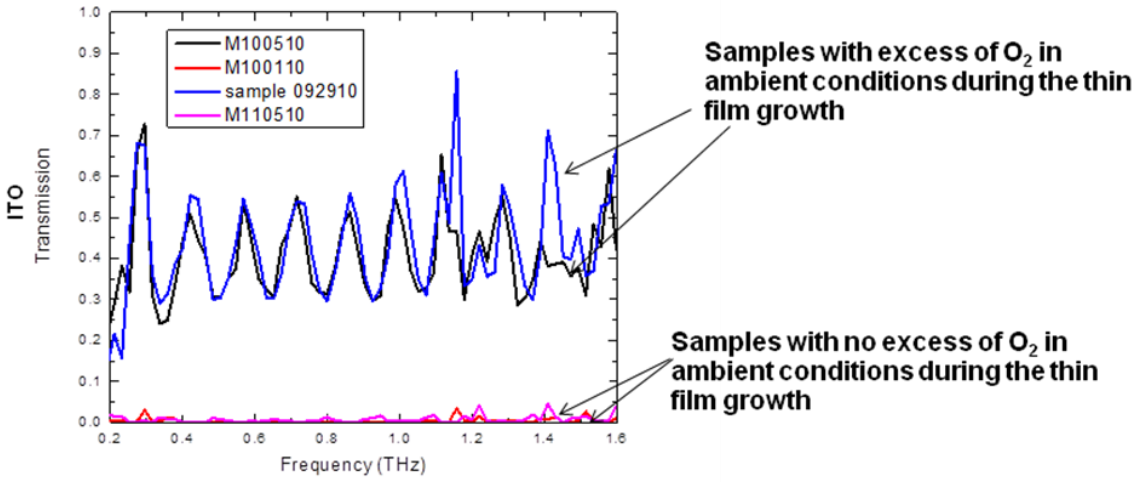

Fig. 4.13 Transmission terahertz spectroscopy of ITO

4.7 Conclusion

The overarching goal of this part of the DSI—namely, demonstration of a tunable metamaterial surface in the terahertz spectrum of radiation—has been achieved. This tunable metamaterial surface will enable the design and fabrication of active metamaterial devices in the terahertz spectrum. The architecture of the metamaterial surface designed by the team allows for easy transformation from a single negative to a double negative device. A numerical model has been devised to match the experimental data and determine the dielectric constant of BST. Alternatively, this model can be used to determine the resonant frequency of the device in the terahertz spectrum. In addition, an investigation of the resonant peak shift when the DC bias is applied with the model, and matching this shift with the one obtained from experimental measurements, yielded the first measurement of BST thin film tunability in the terahertz spectrum up to the bias of 6 V. Experimental investigation of the designed metamaterial device also showed polarization dependence of terahertz transmission through the device.

5. Radio Frequency Metamaterial Research

A Zaghloul, T Anthony, and SJ Weiss (*E&RF, SEDD*)

RF metamaterial research is focused on characterizing metamaterial properties at frequency bands of interest to Army applications. Although the characterization analysis is scalable in frequency, the work is mainly presented at the Ku-band. For most of the analysis and measurements, the metamaterial structure is based on the unit cell of capacitively loaded loop (CLL). This cell has been shown to produce negative permeability in part of the frequency band. When combined with a probe or wire, which is known to produce negative permittivity in part of the band, a negative refractive index results in the medium. The cells are arranged in periodic or random patterns, and each has certain properties that are studied. An insight into the mechanism of the negative refraction provides a physical explanation of this property under certain conditions in the wave propagation in the material. The work discussed in this section has been reported in a number of conference papers and presentations,[1–9] an invention disclosure application (pending),[10] technical notes,[11–13] and a master's thesis[14]. References to these publications are made, as appropriate, in the following subsections.

5.1 Capacitively Loaded Loop/Probe (CLL-P) Cell

Metamaterial cells that consist of metalized CLLs printed on dielectric substrate constitute the main design used in this work. CLL is similar in function to the split-ring resonator (SRR), as it operates on the permeability of the material through coupling to the magnetic field. It was widely used in the literature to realize negative permeability. The basic cell is shown in Fig. 5.1a. A metallic wire or probe, on the other hand, oriented in parallel to the electric field operates on the permittivity of the material and was used to realize negative permittivity at narrow frequency bands. The combination of the CLL and the probe, called CLL-P, is shown in Fig. 5.1b.

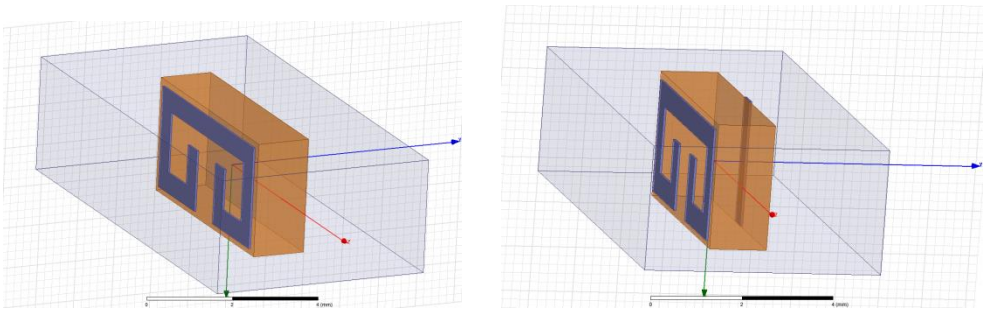

Fig. 5.1 a) Capactively loaded loop (CLL) and b) CLL plus probe (CLL-P) unit cells in parallel orientations

The simulation of the metamaterial cells, arranged on a periodic lattice with certain overall slab dimensions in the x, y, and z directions, can be time and memory consuming using a full-wave analysis tool. Instead, the cell can be simulated with the orientation in Fig. 5.1 with a wave propagating in the z direction (red in figures) and with the electric field oriented in the x direction (blue, downward in figures). The top and bottom yz planes are perfect electric-conducting (PEC) planes, and the side xz planes are perfect magnetic-conducting (PMC) planes. This simulates a parallel-plate waveguide structure with the corresponding images of the unit cell forming an infinite array in the xy plane with 2-dimensional spacing corresponding to the locations of the PEC and PMC planes. The orientation of the CLL-P unit cell parallel to the propagation direction is referred to as *parallel orientation*. Figure 5.2 shows the cell oriented perpendicular to the propagation direction (z) and is referred to as *perpendicular orientation*. The electric field remains in the x direction, and the propagation is in the z direction.

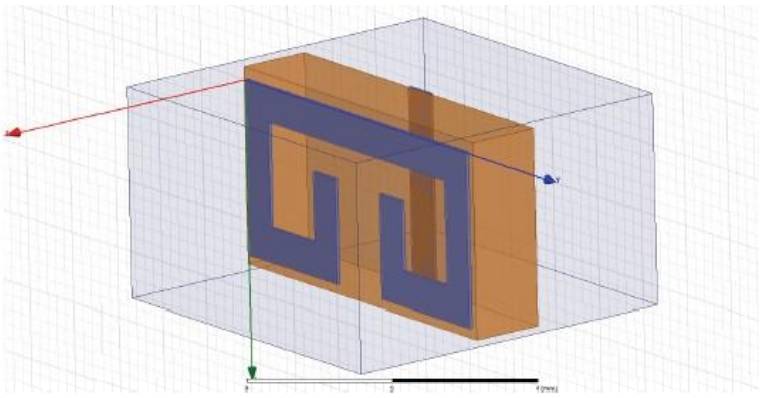

Fig. 5.2 CLL plus probe (CLL-P) unit cells in perpendicular orientation

The simulation results for different cell structures and orientations are shown in Figs. 5.3–5.10.[4,14] The amplitude and phase of the S parameters, S_{11} and S_{21}, are shown first. This is followed by a quad chart, showing the material impedance, refractive index, permittivity, and permeability. All are shown as complex numbers and are calculated in the range of 0–15 GHz.

The first case, shown in Figs. 5.3 and 5.4, is for CLL unit cells without the wire or probe, as depicted in Fig. 5.1a. The cell orientation is for parallel propagation. This case indicates that the CLL affects the permeability of the material, such that it becomes a negative narrow bandwidth close to 7 GHz. It also affects amplitudes and phases of other parameters around the same frequency. The refractive index goes below unity, and the phases of the scattering parameters show inflection that results from and causes these effects. Adding the probe or short wire on the other side of a substrate with a length less than the full height of the loop is referred to as a *cut-wire addition*. This changes the characteristics of the material, as shown in Figs. 5.5 and 5.6 in a similar manner as the CLL-only case. When the length of the wire increases to become continuous wire behind stacked CLLs, a negative refraction index starts to appear over the narrow frequency band. This case is shown in Figs. 5.7 and 5.8. In all 3 cases so far, the propagation of the signal through the material is assumed to be in the parallel direction, with the length of the loop aligned with the propagation direction.

When the propagation is in the direction perpendicular to the CLL plane, as shown in Fig. 5.2, the inflection point moves up in frequency to around 14 GHz. This is shown in Figs. 5.9 and 5.10. Here the permeability and permittivity show negative values over a narrow band, and a wider negative refraction band appears around the same frequency. As seen later in the next subsection, combining the parallel and perpendicular arrangements of the CLL cells produce a cross-cell that shows negative refraction in the experimental setup. The results of this simulation indicate that the parameters, dimensions, and the inclusion of the probe or wire behind the CLL layer in parallel and/or perpendicular arrangements affect the material constitutive parameters to produce values that may not be available in natural or composite materials.

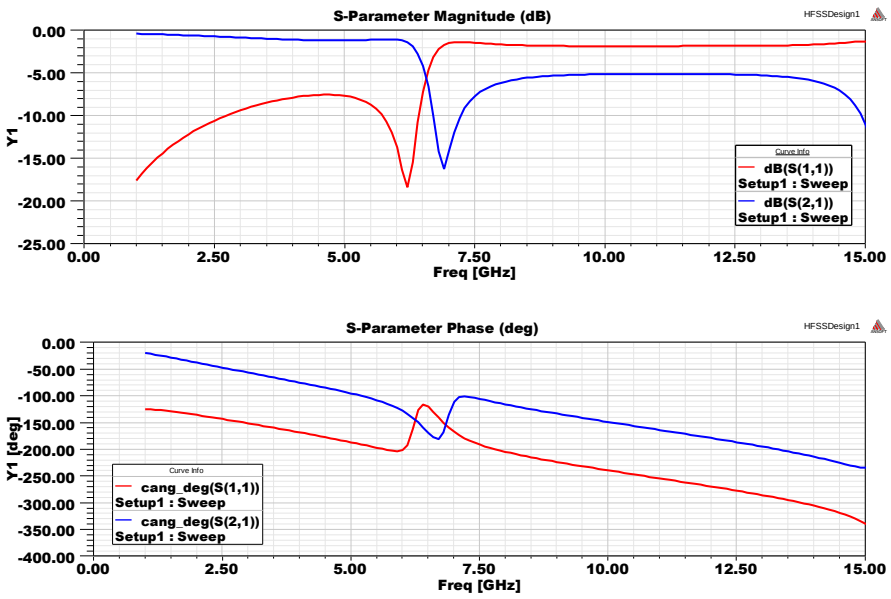

Fig. 5.3 S parameters, magnitude, and phase for CLL cells without probes: parallel orientation

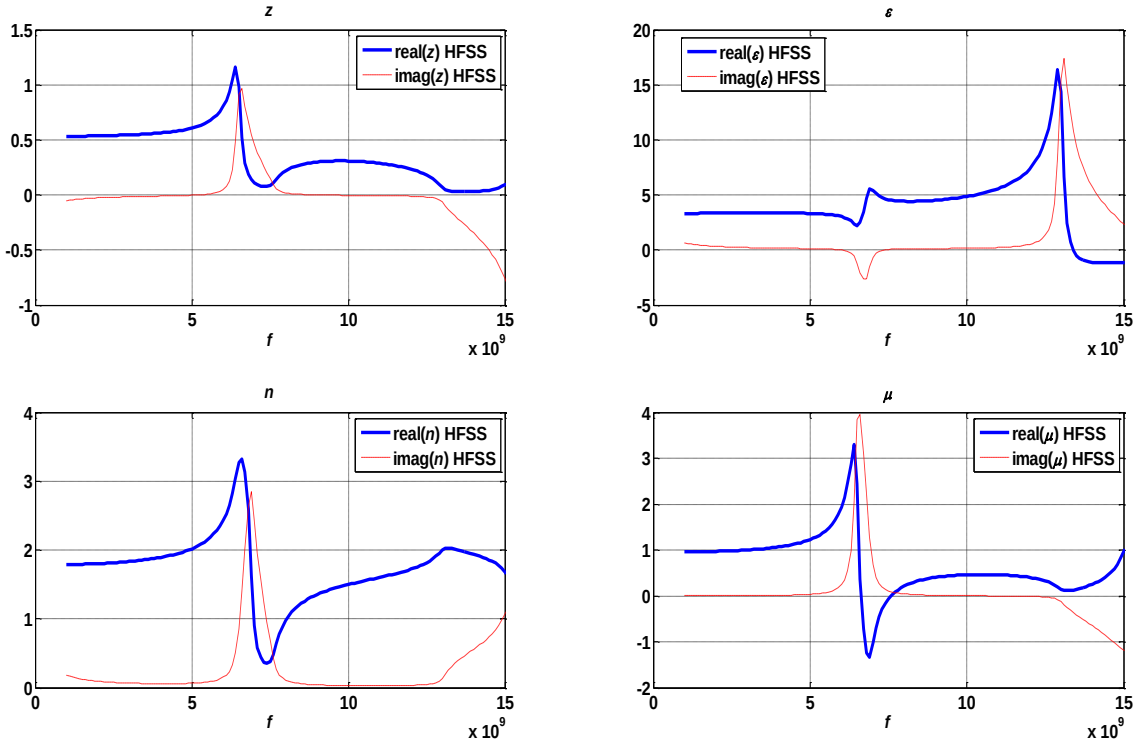

Fig. 5.4 Material impedance, refractive index, permittivity, and permeability for CLL cells without probes: parallel orientation

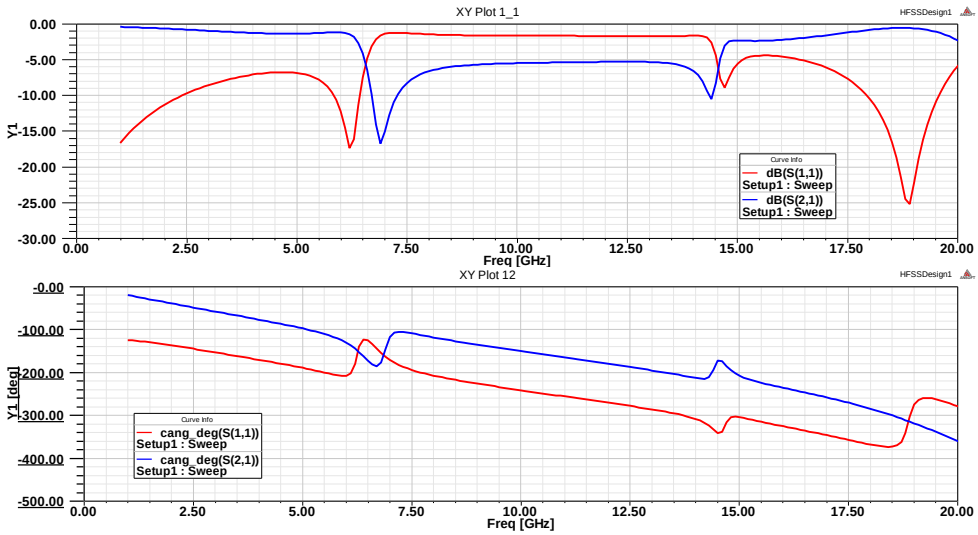

Fig. 5.5 S parameters, magnitude, and phase for CLL cells with probes of cut wires: parallel orientation

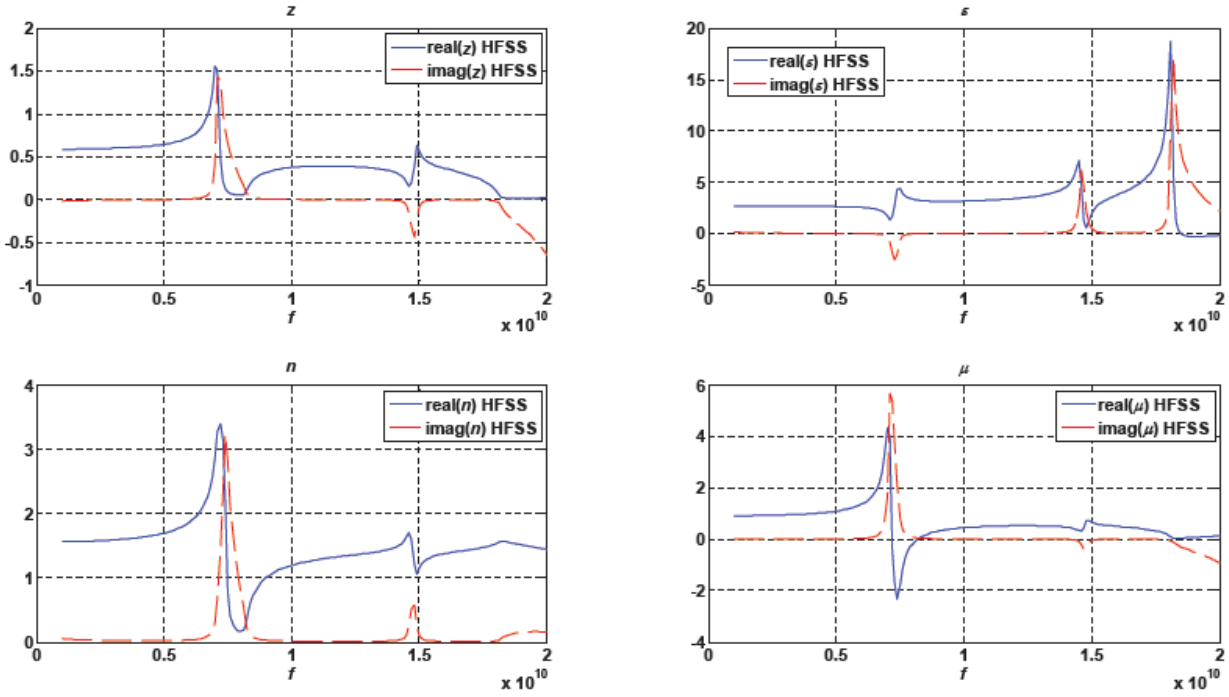

Fig. 5.6 Material impedance, refractive index, permittivity, and permeability for CLL cells with probes of cut wires: parallel orientation

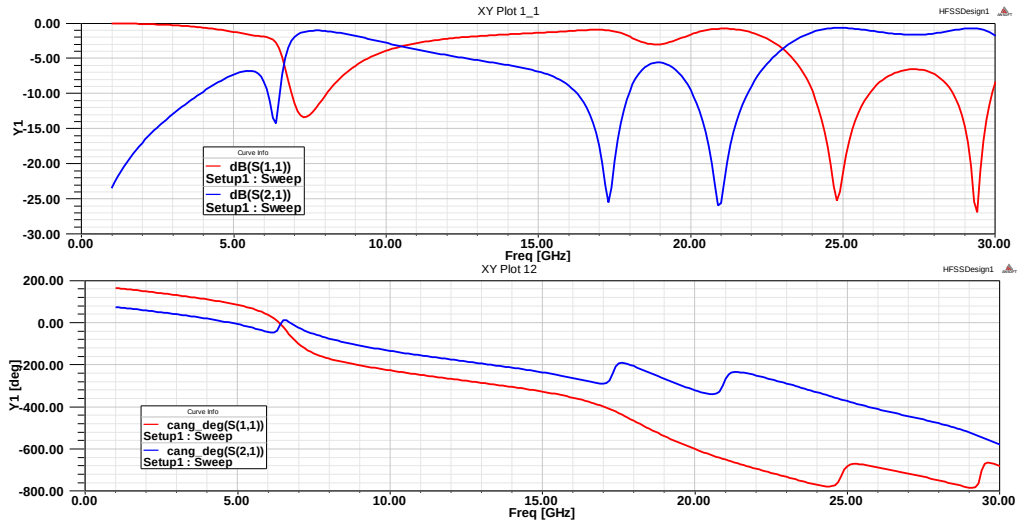

Fig. 5.7 S parameters, magnitude, and phase for CLL cells with probes of continuous wires: parallel orientation

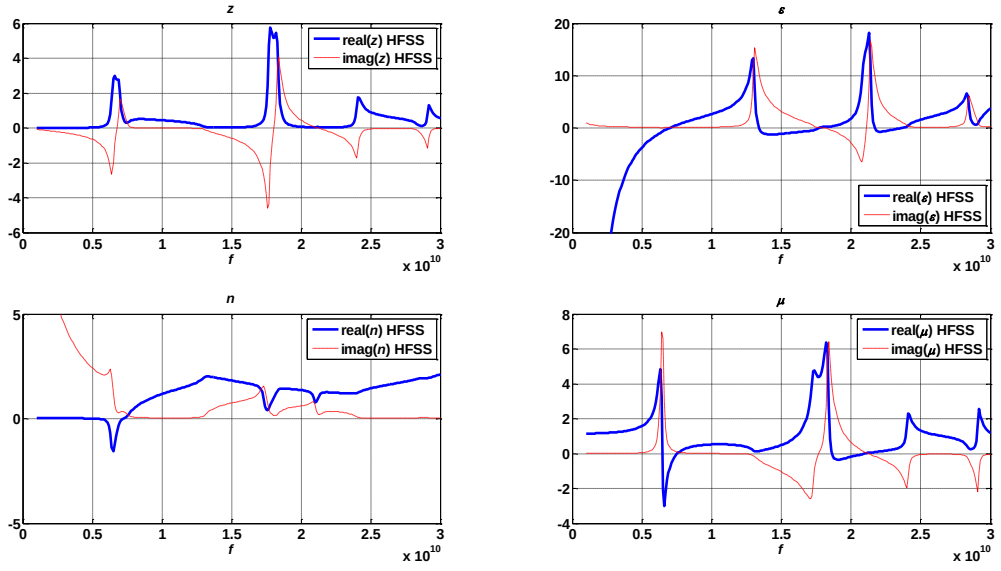

Fig. 5.8 Material impedance, refractive index, permittivity, and permeability for CLL cells with probes of continuous wires: parallel orientation

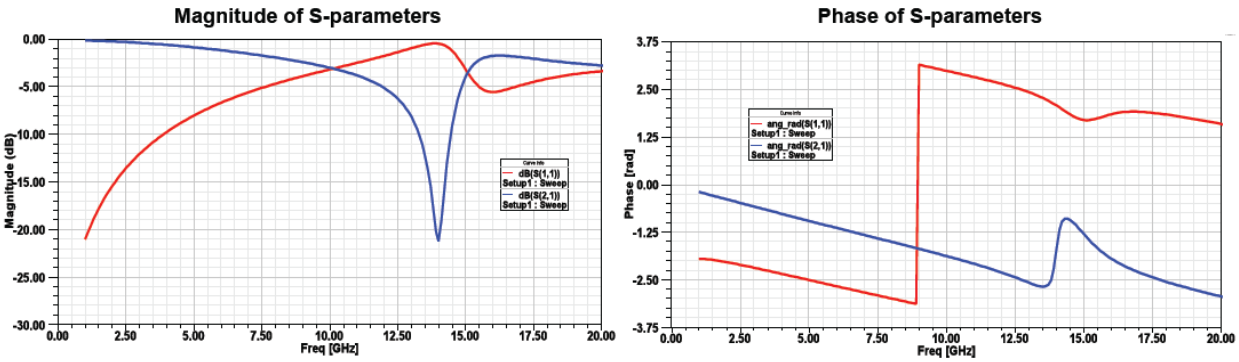

Fig. 5.9 S parameters, magnitude, and phase for CLL cells with probes of continuous wires: perpendicular orientation

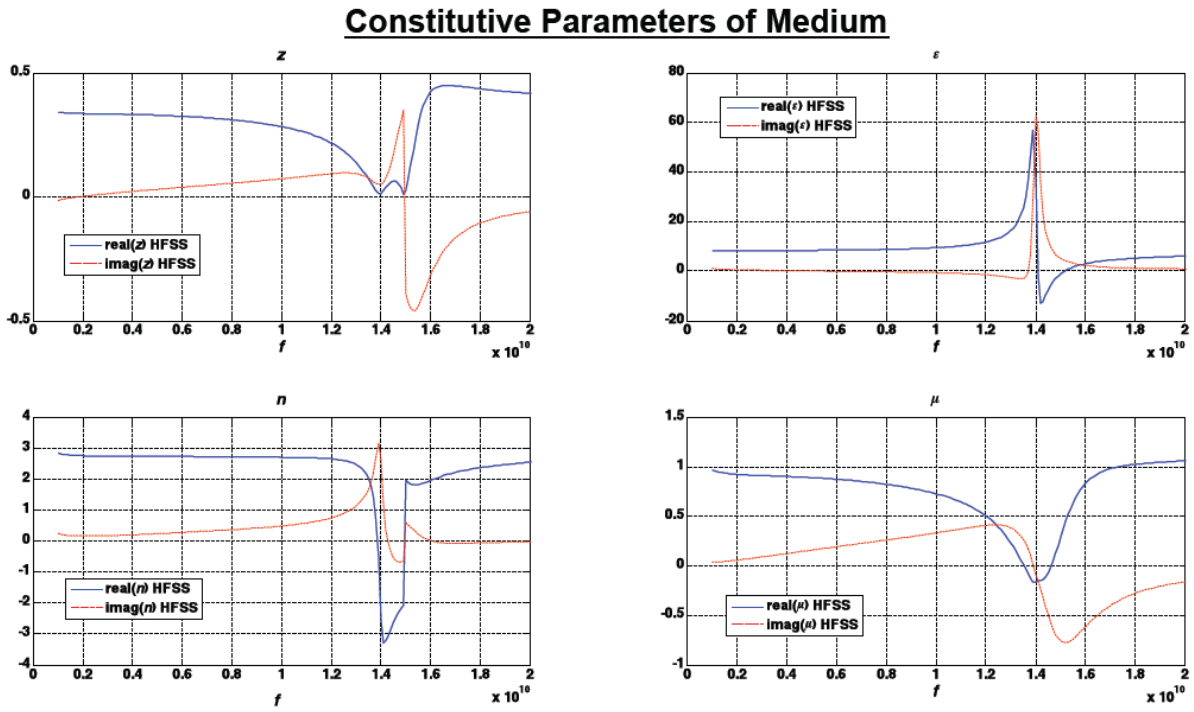

Fig. 5.10 Material impedance, refractive index, permittivity, and permeability for CLL cells with probes of continuous wires: perpendicular orientation

5.2 Random Capacitively Loaded Loop/Probe (CLL-P) Arrangement

As noticed in the periodic arrangement of the CLL and CLL-P cells that are simulated using a single cell in PEC and PMC boundaries, the material characteristics have inflection points and, in some cases, negative constitutive parameters and negative refraction coefficients over a narrow frequency band. It was hypothesized that if the unit cells are arranged at random, their density in a

specific volume would be less, resulting in lower losses, and the lack of periodicity would increase the bandwidth of the inflection region that leads to negative refraction in some cases would increase. Simulation of such random arrangements is shown in this subsection,[4] while measurements of fabricated random, as well as periodic, materials are shown in the next subsection. By the nature of its structure and the lack of continuity in the wire or probe elements of the cell, the random arrangement of the CLL-P cells is limited to the cut-wire case. This limits, and may eliminate, the frequency band over which the negative refraction occurs. Figure 5.11 shows a 3-dimensional (3-D) random arrangement of CLL cells. Figure 5.12 shows the case of random arrangements in the planes of layered 2-dimensional (2-D) material. The direction of propagation is neither parallel nor perpendicular in the 3-D arrangement, and is more perpendicular than parallel in the planar 2-D arrangement. The simulation results, represented by the scattering matrix parameters S_{11} and S_{21} for a multilayer 2-D random material, are shown in Fig. 5.13. The figure shows a distinct region in the frequency domain where the inflection in phase appears. The frequency band over which the S parameters are different is identified. More studies and simulations are needed, along with statistical analyses of the constitutive parameters and refractive index of the material.[5] The measured results in the next subsection identify the frequency band over which the material behaves differently, but conclusions cannot be derived from the measurements either.

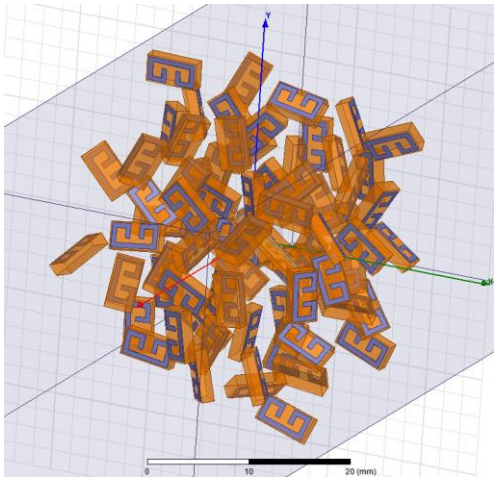

Fig. 5.11 Three-dimensional random arrangement of CLL cells

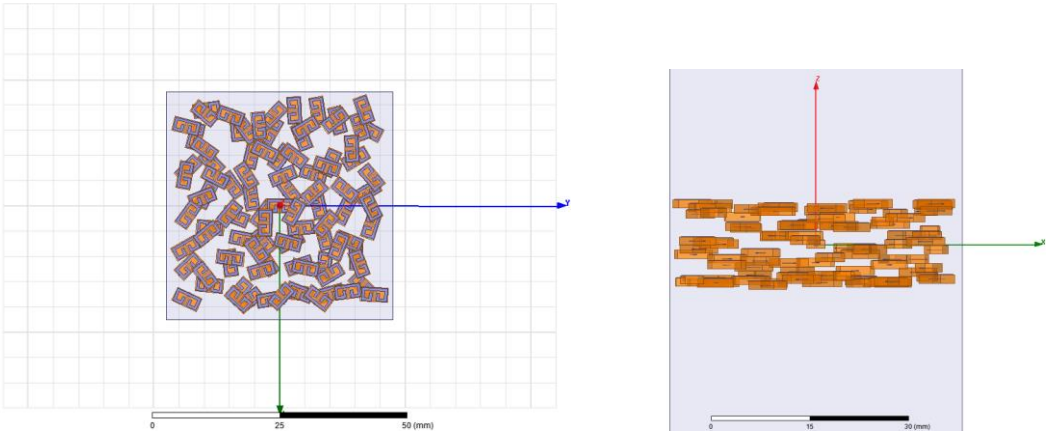

Fig. 5.12 Two-dimensional random arrangement of CLL cells forming a slab: (left) top view of one layer and (right) side view showing 2-D layers

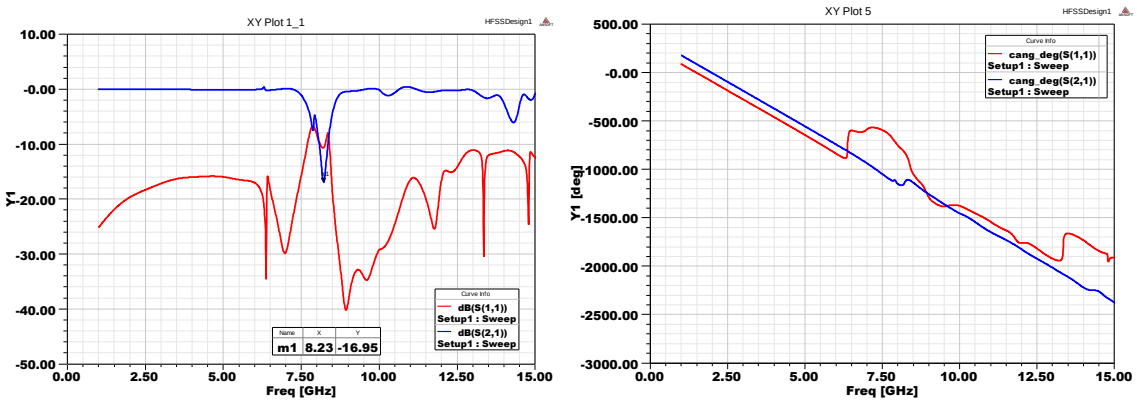

Fig. 5.13 Magnitude (left) and phase (right) of S_{11} (red) and S_{21} (blue) for a layered 2-D random metamaterial of CLL-P cells

5.3 Measurements of CLL-P Metamaterial Slabs

Samples of the CLL-P metamaterial were fabricated and measured to deduce the constitutive parameters and the refractive index of the material.[1,3] Both periodic and random arrangements were assembled in different blocks, primarily in the form of a slab of specific dimensions. The periodic arrangement was set in the cross-configuration, which has the CLL-P cells forming orthogonal parallel and perpendicular planes as defined above. The cell used in the random arrangement is cut in a cylindrical shape to allow for high-density packing and separated CLL-P printed cells at the same time. Figure 5.14 shows sketches of the cell definition for both the periodic and random arrangements. Fabricated parts in Fig. 5.15 show the orthogonal layers in the periodic arrangement and the high-density packing of cells in the random one.

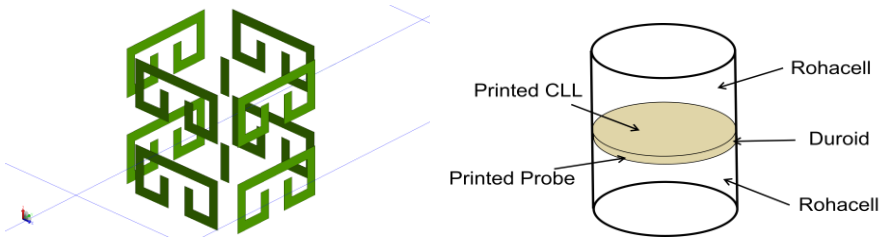

Fig. 5.14 Unit cell of fabricated CLL-P periodic (left) and random (right) metamaterial with cut wire probes

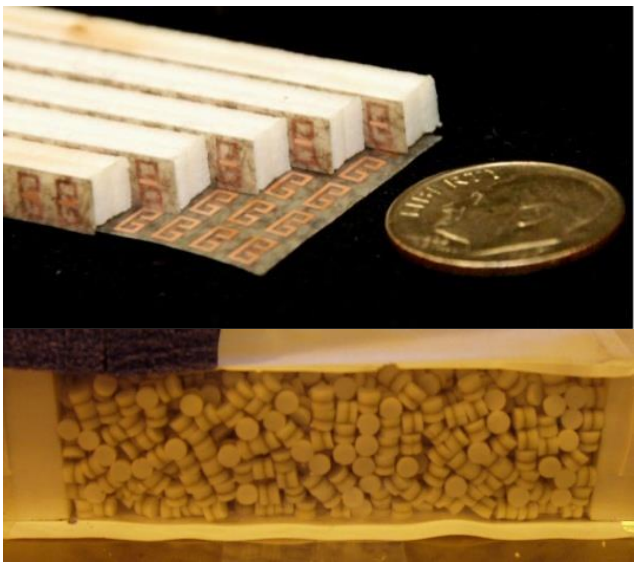

Fig. 5.15 Picture of fabricated CLL-P metamaterial in periodic (top) and 3-D random arrangements

A sketch of the experimental setup is shown in Fig. 5.16. A transmitter and receiver are placed across from each other around a circular turntable that houses the metamaterial slab. Narrow-beam horns are used on both sides to suppress undesired interference and reflections. The metamaterial slab is surrounded by sheets of absorbing material to limit the diffraction of the radiation from the transmitter to the receiver. The rotation of the transmitter allows for testing the material over a wide variation of incident angles. A picture of the setup is shown in Fig. 5.17. An upper plate hinged to the lower plate of the turntable, and of the same size, allows for creating a parallel plate waveguide environment for the metamaterial testing.

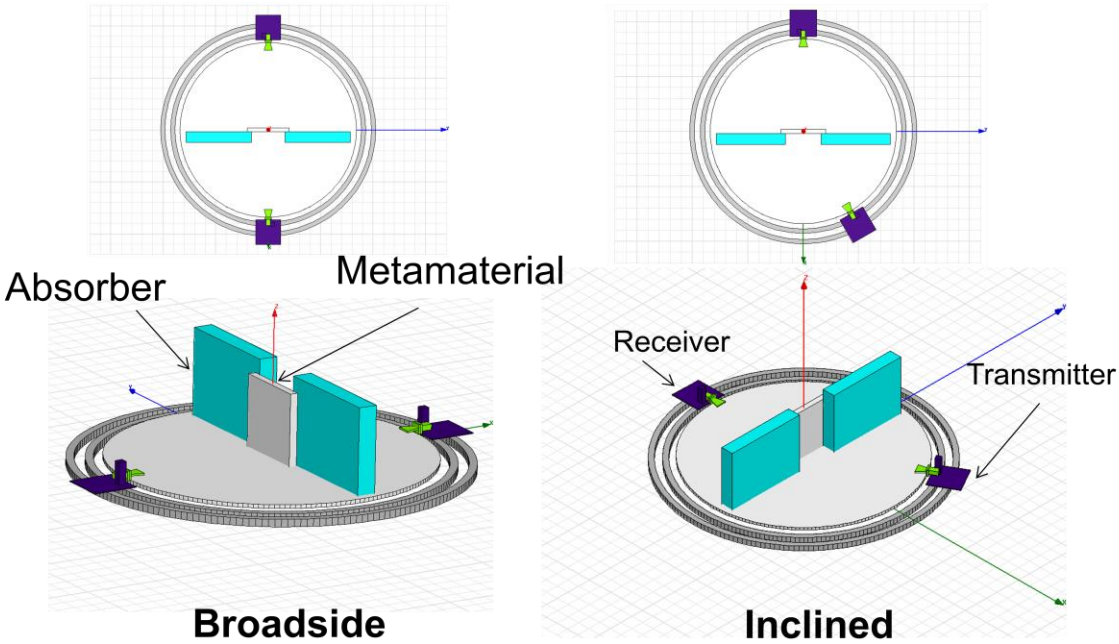

Fig. 5.16 Sketch of the measurement setup to study the transmission, reflection, and refraction performance of the metamaterial slab for boresight and inclined incidence

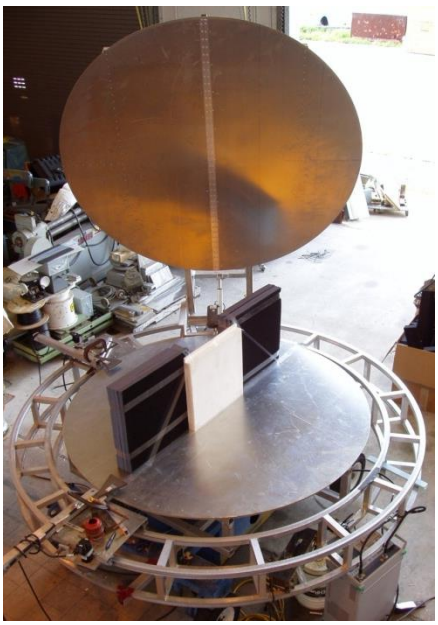

Fig. 5.17 Picture of the measurement setup designed with optional upper plate for parallel-plate waveguide transmission

The results reported in this subsection are for the case with the upper plate lifted, as shown in Fig. 5.17, as the parallel plate environment was proven to be hard to control with the plate sizes at the frequency of measurements.[2] Scattering matrix parameters, in an amplitude phase, were recorded and used to derive the refractive index of the material and the corresponding constitutive parameters. The angular location of the peak level of radiation as detected by the receive horn for different inclined transmit angles was also used to determine the refractive index of the material. Phase measurements were a key element in the accuracy of predicting the constitutive parameters from the scattering matrix data. Samples of the measured results are shown in Figs. 5.18 and 5.19 for the refractive index and scattering parameters, respectively. This is shown for both periodic and random metamaterials composed of CLL-P cells.

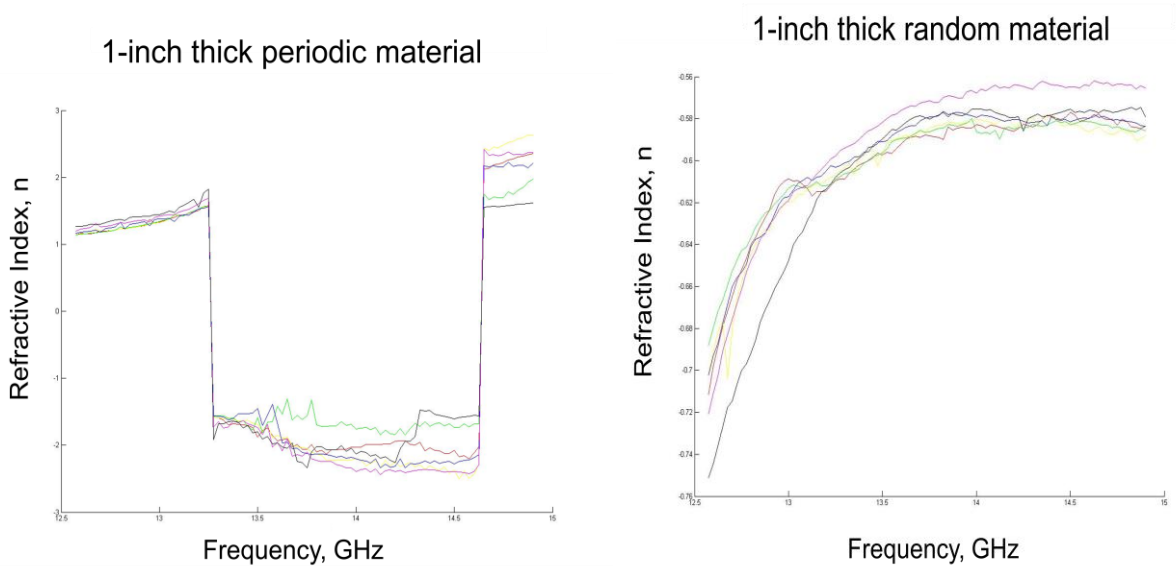

Fig. 5.18 Refractive index for periodic and random structures as deduced from measured transmission and refraction phases

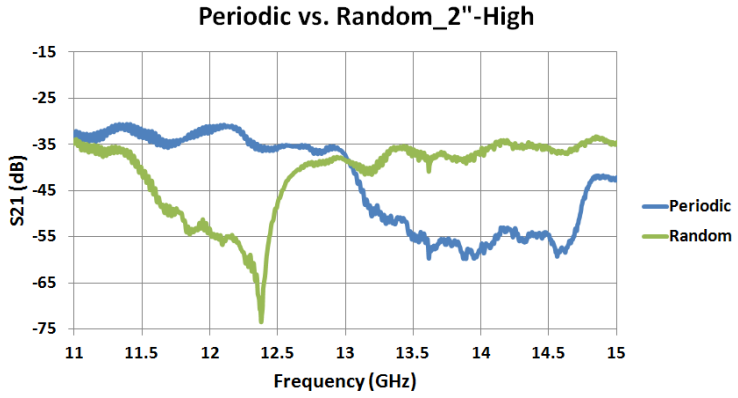

Fig. 5.19 Transmission parameter S_{21} for periodic and random slabs, showing the shift in bandwidth

5.4 Remarks on Metamaterial Characterization

The characterization of metamaterials was performed through simulation and measurements for both periodic and random arrangements of CLL and CLL-P unit cells. As mentioned earlier, some of the results are not conclusive. Rigorous electromagnetic analysis has been performed on general forms of metamaterial cells.[11–13] Comparison of such analysis and correlating it to the results shown here are underway. Also, circuit models have been devised to analyze metamaterials. This also needs to be performed for the CLL-P-based material.

Of interest is the phase response of propagation through the metamaterial. It is conjectured that the unit cell structure causes the transmission phase to be large at certain frequency bands.[8] At inclined incidence, this translates in imposing steep phase progression across the wavefront as the signal passes through the material. The phase progression results in the creation of a grating lobe in the visible region, hence the appearance of a beam in the negative refraction direction. This is proven analytically using conventional array theories. A study of the presence of this phase progression for the metamaterials in question is underway.

5.5 Application of CLL Metamaterials to Dipole Antenna Enhancement

As pointed out earlier, the CLL cells contribute to changing the permeability of the medium. High-permeability material can form a surface or a block of metamaterial that reflects a wave coherently at a small distance. This can be used to produce a high-gain narrow beam from a conventional dipole.[6,7,10] Two sides of the CLL plane can act as a reflector and a director around the dipole in a fashion similar to a Yagi-Uda array. If multiple planes are placed to surround the dipole, as shown in Fig. 5.20, a sharp, high-gain beam results. The beam can be steered mechanically by rotating the CLL structure around the dipole.

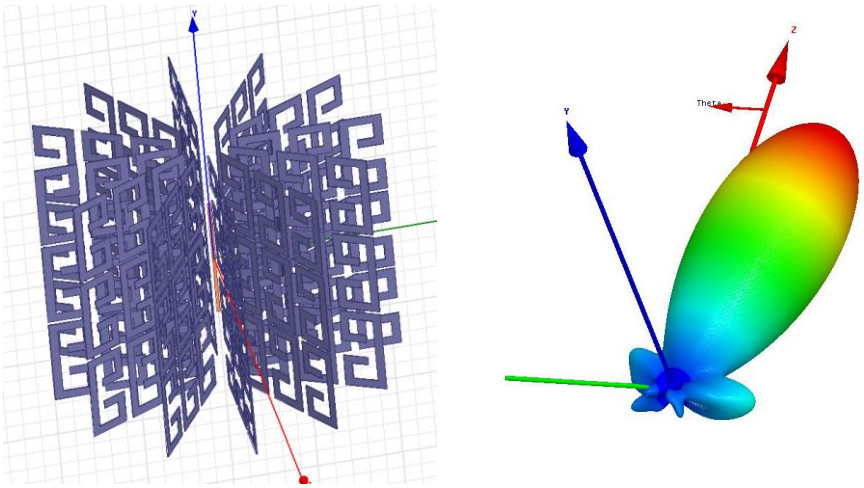

Fig. 5.20 Metamaterial-enhanced dipole using multiple planes of CLL cells and sharp high-gain beam

This concept of enhancing the performance of a dipole using metamaterial loading was verified experimentally in a planar structure. The fabricated dipole structure is shown in Figure 5.21. Simulated and measured results for this planar CLL-enhanced dipole are shown in Figs. 5.22 and 5.23, for the return loss and gain performance, respectively. Figure 5.23 also shows the high front-to-back ratio of the enhanced dipole beam. The comparison proves the concept. The measured gain for the conventional dipole with no metamaterials is shown as a reference.

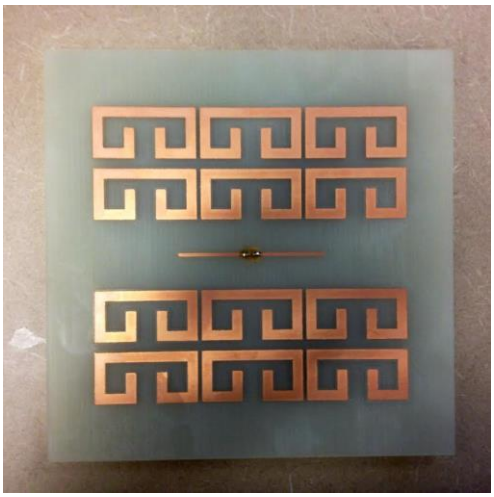

Fig. 5.21 Picture of fabricated planar structure for metamaterial-enhanced dipole

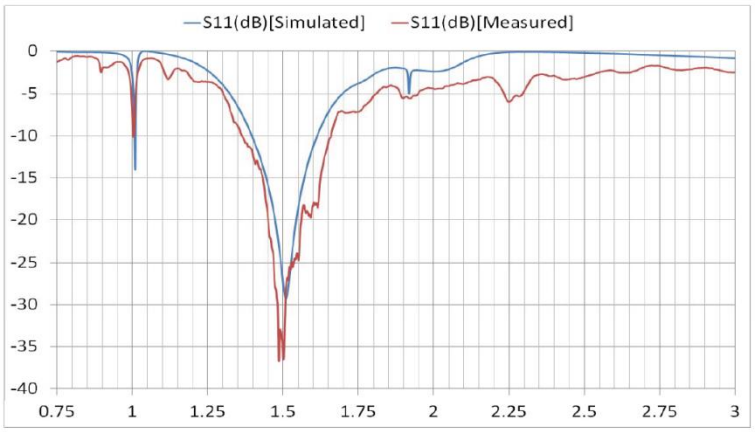

Fig. 5.22 Simulated and measured S_{11} of the planar metamaterial-enhanced dipole

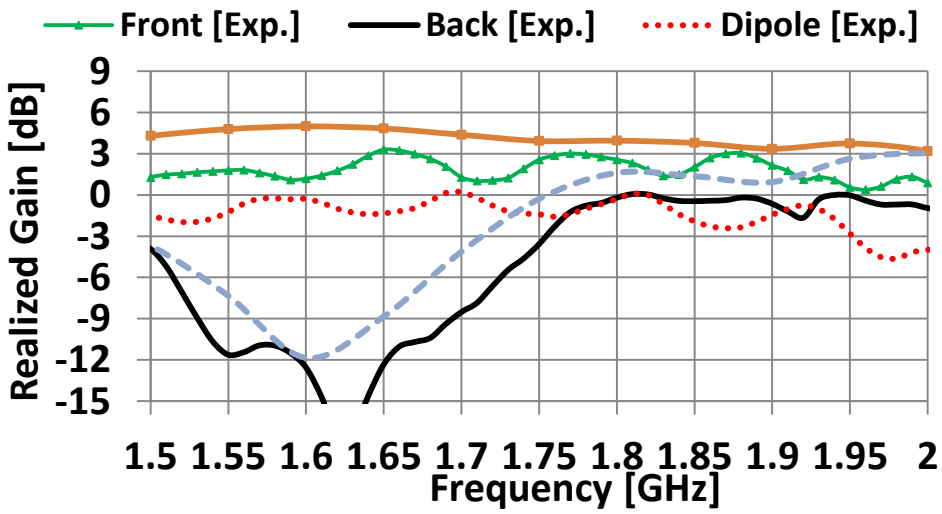

Fig. 5.23 Comparison of measured (green and black) vs. simulated (orange and dashed blue) realized gain and front-to-back ratio of planar metamaterial-enhanced dipole; conventional dipole is also plotted as a reference (dotted red)

5.6 References

1. Zaghloul AI, Lee YM, Anthony T, Weiss SJ. Measurements of metamaterials in a parallel-plate waveguide medium. Antenna Applications Symposium; 2011 Sep; Allerton, IL.

2. Lee Y, Zaghloul AI. Characterization of parallel-plate waveguides for material measurements. URSI National Radio Science Meeting; 2012 Jan; Boulder, CO.

3. Zagloul AI, Weiss SJ, Lee YM, Anthony TK. Characterization of metamaterials through parallel-plate waveguide measurements. META'12. 3rd International Conference on Metamaterials, Photonic Crystals and Plasmonics; 2012 Apr; Paris, France.

4. Hodge J II, Anthony TK, Zaghloul AI. Simulation and analysis of non-periodic and random metamaterial structures. URSI National Radio Science Meeting; 2014 Jan; Boulder, CO.

5. Talalai GA, Zaghloul AI. Problem formulation for randomized metamaterials. CAP-CON; 2014 May; Chantilly, VA.

6. Hodge J II, Anthony TK, Zaghloul AI. Enhancement of the dipole antenna using a capacitively loaded loop (CLL) structure. IEEE International Symposium on Antennas and Propagation; 2014 Jul; Memphis, TN.

7. Hodge J II, Anthony TK, Zaghloul AI. Metamaterial loaded dipole antennas. Antenna Applications Symposium; 2014 Sep; Allerton, IL.

8. Talalai GA, Garner TJ, Weiss SJ, Zaghloul AI. Relationship between phased arrays and negative refraction. Applied Computational Electromagnetics Society (ACES) Conference; 2015 Mar; Williamsburg, VA.

9. Hodge J II, Anthony TK, Zaghloul AI. Utilizing active circuit elements for dynamic tuning and electronic scanning of CLL-loaded dipole antenna structure. USNC-CNC/URSI Meeting; 2015 Jul; Vancouver, BC, Canada.

10. Hodge JA II, Anthony TK, Zaghloul AI. Metamaterial-loaded dipole antenna. Invention disclosure, Pending, ARL, 2015.

11. Talalai GA. Metamaterial Modeling: S-parameter extraction method. Technical Note, CERDEC, August 2013.

12. Talalai GA. Metamaterial modeling: quasi-static approximation. Technical Note, CERDEC, March 2014.

13. Talalai GA. Macroscopic electromagnetic modeling. Technical Note, CERDEC, March 2014.

14. Hhodge J II. Analysis of periodic and random capacitively-loaded loop (CLL) metamaterial structures for antenna enhancement applications [master's thesis]. [Blacksburg (VA)]: Virginia Tech; 2014 May.

6. List of Publications, Patents, and Papers

Papers:

- Zhou W, Dang G, Taysing-Lara M, Chang-Hasain C. Demonstration of a slow-light high-contrast metastructure cage waveguide. Proceedings of the SPIE Photonics West; 2013;8633:863305.
- Zhou W, Dang G, Taysing-Lara M, Karagodsky V, Sun T, Chang-Hasnain C. Slow-light high contrast metastructure hollow-core waveguides. Proceedings of the SPIE Photonics West; 2012;8270–8.
- Zhou W. Slow-light waveguide using high contrast gratings. Summary of 2012-International Nano-Electro-Optics Workshop; 2012.
- Dang G, Taysing-Lara M, Zhou W. Loss measurements in silicon hollow-core waveguides with metastructure high-contrast grating. Proceedings of the 2012 Frontiers in Optics/Laser Science XXVIII (FiO/LS) Meeting; 2012.
- Zaghloul AI. Active reflection phase surfaces for cognitive radar. Proceeding URSI National Radio Science Meeting; 2013.
- Hodge J II, Anthony TK, Zaghloul AI. Simulation and analysis of non-periodic and random metamaterial structures. Proceeding URSI National Radio Science Meeting; 2014.
- Hodge J II, Anthony TK, Zaghloul AI. Enhancement of the dipole antenna using a capacitively loaded loop (CLL) structure. Proceeding of IEEE International Symposium on Antennas and Propagation; 2014.
- Dang G, Taysing-Lara M, Zhou W, Sun T, Yang W, Chang-Hasnain C. Design and fabrication of 3D high-contrast metastructure THz cage waveguides. Proceedings of the SPIE Photonics West; 2015.
- Sun T, Yang W, Zhou W, Chang-Hasnain C. Guided modes and slow light in high contrast grating hollow core waveguide. Optical Society of America, to be published.
- Lee Y, Zaghloul AI. Characterization of parallel-plate waveguides for material measurements, URSI National Radio Science Meeting; 2012 Jan; Boulder, CO.

- Zaghloul AI, Weiss SJ, Lee YM, Anthony TK. Characterization of metamaterials through parallel-plate waveguide measurement. META'12; 3rd International Conference on Metamaterials, Photonic Crystals and Plasmonics; 2012 Apr; Paris, France.
- Talalai GA, Zaghloul AI. Problem formulation for randomized metamaterials. CAP-CON; 2014 May; Chantilly, VA.
- Hodge J II, Anthony TK, Zaghloul AI. Metamaterial loaded dipole antennas. Antenna Applications Symposium; 2014 Sep; Allerton, IL.
- Talalai A, Garner TJ, Weiss SJ, Zaghloul AI. Relationship between phased arrays and negative refraction. Applied Computational Electromagnetics Society (ACES) Conference; 2015 Mar; Williamsburg, VA.
- Hodge J II, Anthony TK, Zaghloul AI. Utilizing active circuit elements for dynamic tuning and electronic scanning of CLL-loaded dipole antenna structur. USNC-CNC/URSI Meeting; 2015 Jul; Vancouver, BC, Canada.

Presentations (incomplete list):

- Dang G, Taysing-Lara M, Zhou W, Sun T, Yang W, Chang-Hasnain C. Design and fabrication of 3D high-contrast metastructure THz cage waveguides. Photonics West, 2015.
- Zhou W, Dang G, Taysing-Lara M, Chang-Hasnain C. Demonstration of a slow-light high-contrast metastructure cage waveguide. Photonics West, 8633-05, 2013.
- Zhou W et al. Slow-light high contrast metastructure hollow-core waveguides. Photonics West, 8270–8, 2012.
- Zhou W. Slow-light waveguide using high contrast gratings. Summary of 2012 International Nano-Electro-Optics Workshop, 2012.
- Chang-Hasnain C. High-contrast metastructures for integrated optics. Opto Plenary Session, Photonics West, 2012.
- Dang G, Taysing-Lara M, Zhou W. Loss measurements in silicon hollow-core waveguides with metastructure high-contrast grating. Frontiers in Optics/Laser Science XXVIII (FiO/LS) meeting. 2012 Oct 14–18; Rochester, NY.
- Zaghloul A. Active reflection phase surfaces for cognitive radar. NRSM USNC-URSI Conference. 2013 Jan 8–11; Boulder, CO.

Patents:

- Zhou W. Method of constructing a semiconductor hollow-core waveguide using high-contrast gratings. United States patent US patent 8,532,486. 2013 Sep 10.
- Hodge JA II, Anthony TK, Zaghloul AI. Metamaterial-loaded dipole antenna. Invention Disclosure, Pending, ARL, 2015.

Press Release:

- High-contrast gratings forge ultralow-loss, slow-light waveguide. World News, Laser Focus World, April 2012.

1 (PDF) DEFENSE TECH INFO CTR
ATTN DTIC OCA

2 (PDF) US ARMY RSRCH LAB
ATTN IMAL HRA MAIL & RECORDS MGMT
ATTN RDRL CIO LL TECHL LIB

1 (PDF) GOVT PRNTG OFC
ATTN A MALHOTRA

8 (PDF) US ARMY RSRCH LAB
RDRL SE
G METCALFE
RDRL SEE E
G DANG
M TAYSING-LARA
W ZHOU
RDRL SER M
A ZAGHLOOL
RDRL WMM E
E NGO
M IVILL
D SHREIBER